International Journal of Applied Earth Observation and Geoinformation 32 (2014) 1–18

Contents lists available at ScienceDirect

International Journal of Applied Earth Observation and Geoinformation

journal homepage: www.elsevier.com/locate/jag

Image-based correlation of Laser Scanning point cloud time series for landslide monitoring

Julien Travelletti[a,b], Jean-Philippe Malet[a,*], Christophe Delacourt[c]

[a] Institut de Physique du Globe de Strasbourg, CNRS UMR 7516, Université de Strasbourg/EOST, 5 rue René Descartes, 67084 Strasbourg Cedex, France
[b] BEG, Bureau d'Etudes Géologiques SA, Rue de la Printse 4, 1994 Aproz, Switzerland
[c] Université Européenne de Bretagne, Institut Universitaire de la Mer, CNRS UMR 6538, Université de Brest, Brest, France

ARTICLE INFO

Article history:
Received 26 October 2013
Accepted 20 March 2014
Available online 19 April 2014

Keywords:
Terrestrial Laser Scanning
Point clouds
Image correlation
Landslide
Kinematics
Strain analysis

ABSTRACT

Very high resolution monitoring of landslide kinematics is an important aspect for a physical understanding of the failure mechanisms and for quantifying the associated hazard. In the last decade, the potential of Terrestrial Laser Scanning (TLS) to monitor slow-moving landslides has been largely demonstrated but accurate processing methods are still needed to extract useful information available in point cloud time series. This work presents an approach to measure the 3D deformation and displacement patterns from repeated TLS surveys. The method is based on the simplification of a 3D matching problem in a 2D matching problem by using a 2D statistical normalized cross-correlation function. The computed displacement amplitudes are compared to displacements (1) calculated with the classical approach of Iterative Closest Point and (2) measured from repeated dGPS observations. The performance of the method is tested on a 3 years dataset acquired at the Super-Sauze landslide (South French Alps). The observed landslide displacements are heterogeneous in time and space. Within the landslide, sub-areas presenting different deformation patterns (extension, compression) are detected by a strain analysis. It is demonstrated that pore water pressure changes within the landslide is the main controlling factor of the kinematics.

1. Introduction

Slope monitoring techniques have made a lot of progress in the last decade, especially in the field of ground-based remote sensing platforms (e.g. Ground-Based Synthetic Aperture Radar Interferometry – GB-InSAR, Terrestrial Laser Scanning – TLS, Terrestrial Optical Photogrammetry – TOP). These techniques allow to discriminate stable and unstable slope portions from safe and remote places and to map sectors with different kinematics within a landslide body (Delacourt et al., 2007). These instruments provide the necessary information to analyze quantitatively the slope kinematics (e.g. displacement and deformation fields) and propose a geomechanical understanding of the failure mechanisms (Casson et al., 2005; Teza et al., 2008; Oppikofer et al., 2008). This work focuses on the use of repeated Terrestrial Laser Scanning (TLS) surveys. This type of instrument is currently used in a large variety of applications in earth and environmental sciences, and among them for landslide analysis as underlined by the considerable increase in the number of publications in the last years (Slob and Hack, 2004; Sturzenegger and Stead, 2009; Jaboyedoff et al., 2012). TLS instruments allow a fast (typically thousands of points per seconds), distributed, high resolution (millimetric to centimetric) and dense (several millions) acquisition of 3D information of the terrain through point cloud of 3D point locations and near-infrared reflectance intensity (e.g. *X*, *Y*, *Z*, *I*).

The instruments typically use 'time-of-flight' (also known as 'pulse-based'), 'phase-based' or 'waveform processing' technology to determine the distance to the targets. The differences in laser light wavelengths, amount and velocity of point data collection, field acquisition procedures, data processing and possible error sources are detailed in Hiremagalur et al. (2007) and in Vosselman and Maas (2010).

Time-of-flight scanners are the most common type of instruments used in geophysical applications because of their longer distance range (typically 100–800 m) and their possible high acquisition frequency. They combine a pulsed laser emitting the beam, a mirror deflecting the beam toward the scanned area and an optical receiver subsystem which detects the laser pulse reflected from the object. Since the speed of light is known, the travel time of the laser pulse can be converted to a precise distance measurement (Vosselman and Maas, 2010). The precision of the technique is mainly affected by instrumental errors (mirror orientation inside

* Corresponding author. Tel.: +33 368850036.
E-mail address: jeanphilippe.malet@unistra.fr (J.-P. Malet).

http://dx.doi.org/10.1016/j.jag.2014.03.022
0303-2434/

the scanner), pulse flight-time measurement, laser beam divergence (Petrie and Toth, 2008), point density variations due to surface multiple reflections (Abellán et al., 2009; Hodge et al., 2009) and co-registration of the point clouds (Schürch et al., 2011). The precision is quantified by the standard deviation of each point measurement of typically a centimetric accuracy at a distance range of 100 m (Lichti and Jamtsho, 2006). Taking into account the high spatial density of TLS point clouds, the accuracy of point clouds is higher than the accuracy of single data point measurements (Lindenberg and Pfeifer, 2005).

The usefulness of TLS surveys for the monitoring of geomorphologic processes has been demonstrated in the last years, mainly for defining the structure of rocky slopes susceptible to rockfalls and rockslides (Abellán et al., 2009; Oppikofer et al., 2009; Sturzenegger and Stead, 2009; Kasperski et al., 2010) or for characterizing the dynamics of slow-moving (typically a few centimeters to a few meters per year) slope processes such as ice glaciers (Bauer et al., 2003; Schwalbe et al., 2008; Avian et al., 2009) and landslides (Teza et al., 2007; Prokop and Panholzer, 2009; Travelletti et al., 2008; Aryal et al., 2012). Different techniques exist to analyze the space–time evolution and can be broadly classified in five categories.

Category 1 consists in the analysis of differential Digital Terrain Models (DTMs) and is the most commonly used processing technique to compare different surveys. It is used to quantify accumulation or loss of material (Bitelli et al., 2004; Prokop and Panholzer, 2009; Kasperski et al., 2010; Schürch et al., 2011). This method is not fully adapted for landslide kinematic analysis since it provides only information on changes in the vertical component. Furthermore the interpolation in the horizontal (X–Y) plane implies a significant loss of information initially contained in the original point clouds if the gridded mesh size is coarse.

Category 2 consists in the analysis of point pairs in consecutive point clouds (Oppikofer et al., 2009), and in the calculation of displacement vectors of selected objects. This technique has important limitations as it is very difficult to track exactly the same point in consecutive point clouds. Therefore its precision strongly depends on the point clouds resolution, on the deformation pattern of the tracked objects (rigid, elastic or plastic). Further, this method does not exploit all the geometric information contained in the point clouds, and can represent a fastidious processing task for very large datasets.

Category 3 consists in the analysis of point clouds with shortest distance methods (e.g. for instance the Hausdorff metric) to estimate the differences between two surfaces in every direction (Besl and McKay, 1992; Chen and Medioni, 1992; Oppikofer et al., 2009; Vosselman and Maas, 2010). If average displacement vectors of the landslide are known, the algorithm can be constrained to identify points located in the sliding direction and provide a rough estimation of the magnitude of the displacements (Travelletti et al., 2008). However, the reliability of the computed displacements strongly depends on the slope topography relative to the sliding direction. Therefore this method remains rather qualitative.

Category 4 consists in the analysis of point clouds with the Iterative Closest Point (ICP) and Least Squares 3D Surface Matching methods (LSSM). The ICP (Besl and McKay, 1992) and LSSM (Gruen and Akca, 2005) methods are among the most efficient algorithms for the automatic characterization of 3D displacement fields. Their application to landslide monitoring has been demonstrated by Teza et al. (2008) and Monserrat and Crosetto (2008). Teza et al. (2007) presented an automatic calculation method using an ICP-based piecewise alignment method. The method calculates the roto-translational matrix describing the displacement and the rotation of an object considering a high amount of points. The accuracy of the displacement measure is limited by the presence of shadow zones (unscanned areas) and vegetation or important soil deformation. Because this method uses an iterative procedure to identify the optimal rotation and translational components, it can be relatively time consuming without necessarily any convergence in the calculation.

Finally, category 5 consists in the analysis of high resolution DTMs (computed from the original point clouds) using cross-correlation functions. This method, commonly applied for the analysis of time series of laboratory or field optical images (White et al., 2003) is still poorly exploited to monitor continuously active slope processes (Corripio, 2004; Travelletti et al., 2012). The first application in the literature was proposed by Duffy et al. (2004), who quantified the migration of submarine sand dunes by applying a 2D cross correlation on sun-illuminated values computed on a DTM. The elevation data were measured with a multibeam echo sounder. Because the computed displacement field was shown to be dependent on the azimuth of the virtual sun, slope values of the topography were finally correlated instead of the sun-illuminated values. Duffy and Hughes-Clarke (2005) found that displacement rates computed from the slope values are more robust since there is no extra parameter in the slope calculation. A second application was proposed by Schwalbe et al. (2008) who monitored glacier movements; they developed a method in which the point clouds are projected in a regular horizontal (X–Y) grid. First raster images are defined in such a way that each pixel containing a TLS point is filled with a gray intensity value depending on the relative elevation of the point; then, a 2D cross-correlation function is used to track features between two acquisitions. The morphological structures of the glacier (represented by pixels of different gray intensity values) are iteratively dilated to favor confidence to the pixels containing many TLS information for the correlation procedure. This complex iterative procedure allows minimizing the influence of shadow zones in the correlation computation and improved the determination of the velocity field. A third application is proposed by Aryal et al. (2012) for the analysis of the displacement pattern of the Cleveland Corral landslide; the authors correlated a series of DTMs interpolated from the original point clouds in which the relative elevation values (Z) are computed in the horizontal (X–Y) plane. The authors highlighted the development of lateral shear zones and of a non-rigid behavior of the landslide. This approach allows a continuous spatial estimation of the displacement but is limited to still relatively low displacement rates as it is necessary to preserve a relative similar aspect of the DEMs at the different dates.

The objective of this work is to propose a method to measure the 3D displacement field and to estimate the deformation pattern of landslides using high density repeated TLS point clouds. The aim of the method is to be applicable to large displacements and important changes in the morphology of the slopes.

The method uses a normalized cross-correlation function in order to exploit the full geometrical information available in consecutive point clouds. The hypothesis is that for objects scanned from a unique viewpoint, relatively simple 2D correlation functions as largely used in digital photogrammetry (Debella-Gilo and Kaab, 2011) can be applied on multi-temporal point clouds with an accuracy comparable to complex and time-consuming 3D Surface Matching algorithms. Numerous examples demonstrated the efficiency of 2D correlation functions to detect the displacement field of landslides from satellite, airborne and terrestrial optical images (Casson et al., 2005; LePrince et al., 2008; Travelletti et al., 2012), but only little work has been carried out to develop efficient methodologies for TLS point clouds (Travelletti et al., 2008; Schwalbe et al., 2008; Aryal et al., 2012). The performance of the method is tested on datasets acquired at the Super-Sauze landslide (South French Alps) over a period of three years (October 2007–May 2010).

First, the main geomorphological and kinematical characteristics of the landslide are presented. Second, the principles of the

method are explained. Third, the method is applied to the point clouds time series and its performance is evaluated among other measures of displacement. Fourth, a strain analysis is proposed in order to characterize the deformation and displacement regime of the landslide, and some possible controlling factors are identified.

2. Experimental site: the Super-Sauze landslide

The Super-Sauze landslide (Barcelonnette Basin, around 100 km North of Nice, France) is representative of mudslides developed in the Jurassic clay-shales of the South French Alps. It has developed in Callovo-Oxfordian black marls (Fig. 1A and B), in the upper part of the Sauze torrent characterized by a gully-type morphology. The source area is featured by a fault system affecting the black marls and acting as a predisposing factor for the formation of the scarp in the 1970s. The landslide exhibits cumulated displacements of a few meters per year, and is characterized by continuous movements because of a non-obstructing sloping path and a frequent enrichment of material from the main scarp.

2.1. History of development

In the beginning of the 1970s, structurally-controlled failures occurred in the upper part of the Sauze torrent resulting in an accumulation of large marly rock panels, and in the formation of a main scarp (Fig. 1A). These panels have been progressively weathered and a matrix-supported soil fabric, integrating marly fragments of different size, has developed, filling up progressively gullies (Malet, 2003). In the late 1970s, a rising level of soil accumulation in the gullies is observed (Fig. 1A), with some changes in the rate of displacement according to the presence of obstacles in the torrent channel. In 2007, at the start of the TLS surveys, the landslide extended over a

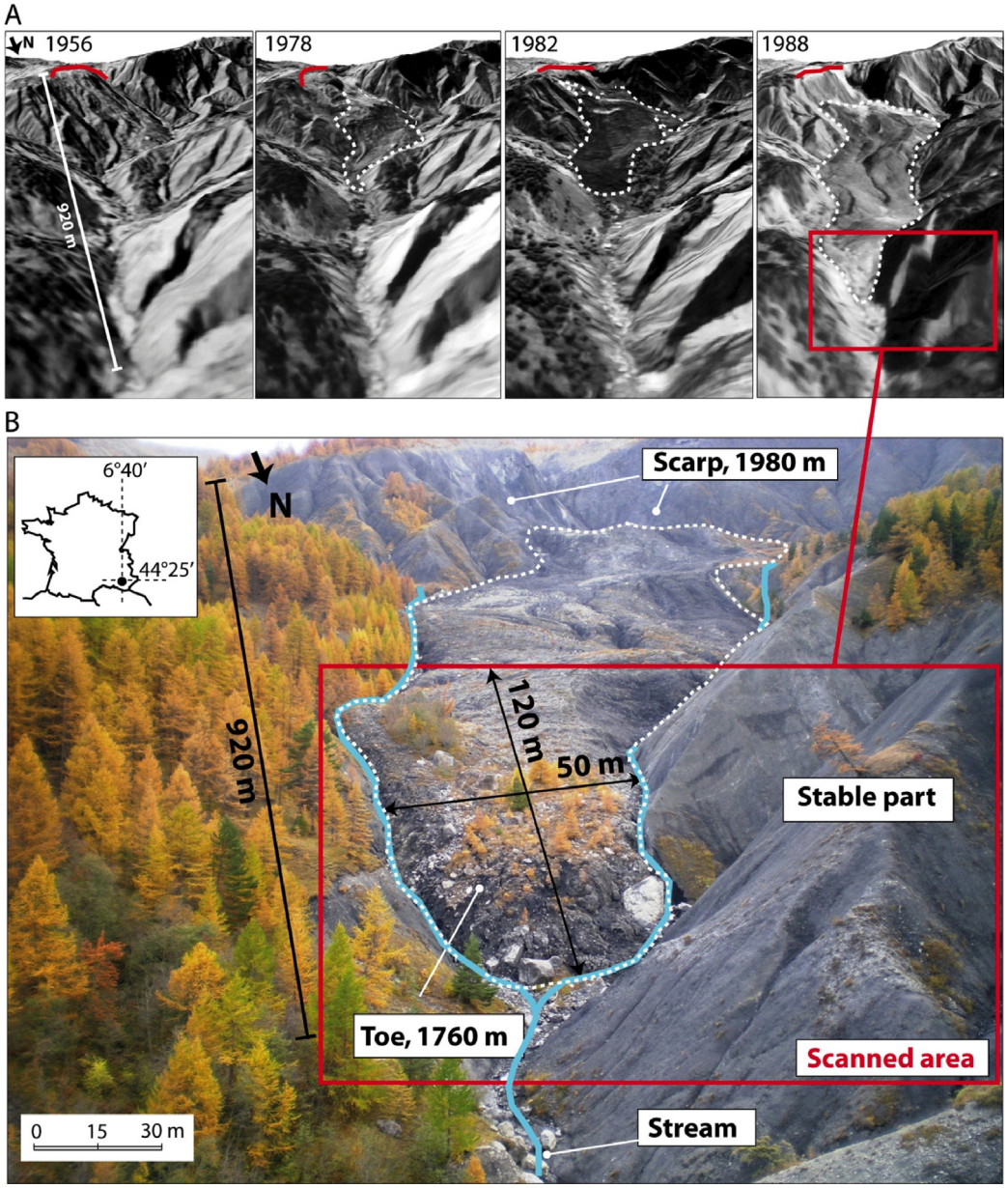

Fig. 1. Morphological setting and evolution of the Super-Sauze landslide. (A) Evolution from 1956 (before failure) to 1988 (adapted from Weber and Herrmann, 2000). The temporary storage of material at the toe of the main scarp and its weathering is clearly recognizable, before the downstream progression of the material in the main channel. (B) Photography of the situation in 2008 where the landslide toe is bordered by two streams. The picture is taken from the TLS base station and corresponds to the plan perpendicular to the viewing direction of the TLS. The toe and a stable slope are included in the scanned area.

horizontal distance of 920 m from the crown (2105 m in elevation) to the toe (1760 m in elevation) with an average 25° slope gradient (Fig. 1B). The landslide bedrock geometry is very complex and its thickness varies between 0 and approximately 20 m, for an estimated total volume of ca. 560,000 m^3 (Travelletti and Malet, 2012). The landslide kinematics is controlled by bedrock geometry, material rheology and hydrology. Morphological features induced by the sliding and flowing mode of the material are easily recognizable and testify of the complex deformation pattern. The contact between the landslide and the stable hillslope (Niethammer et al., 2012) comprises a shear zone of a ca. 5 m in width affected by traction and closely-spaced, sub-parallel and step-like fissures which lie oblique to the main slope direction (e.g. 'en echelon' fissures). Shallow shear surfaces marked by scratches in the direction of movement are easily recognizable at shallow depths. Locally, compression levees and lobes are clearly distinguishable.

2.2. Observed displacement and deformation pattern

The displacements have been monitored since 1996 by different techniques (tacheometry, differential GPS, extensometers; Malet et al., 2002). Since 2007, very-high resolution optical cameras (Travelletti et al., 2012) and three permanent GPS receivers are installed in front and on the landslide, and repeated airborne and TLS surveys are carried out per semesters (Travelletti et al., 2008). The displacement rates vary spatially and temporally in the range of 0.002–0.03 m day^{-1}. Peaks of displacements are related to high pore water pressures in the subsoil (Malet et al., 2005) with possible surface velocities up to 0.4 m day^{-1} in the spring seasons. The displacement magnitude decreases from the upper to the lower parts of the landslide resulting in extension zones in the upper part and the development of compression zones near the toe where the landslide material is accumulating.

The correlation between the displacement rates of two targets (P1 and P2 at the front of the landslide) measured by GPS campaigns and the monthly rainfall for the period 1991–2001 (Fig. 2A) hypothesizes the hydrological control of the kinematics. The differences in the cumulated displacements observed at the upper (P1) and lower (P2) parts of the front indicate a mass accumulation. Even, if the volume accumulated at the front is partly eroded by two lateral streams (Fig. 1B), this erosion rate is not sufficient to counterbalance the progression of the front. Consequently, the position of the front progresses downstream every year with an average velocity of 0.005 to 0.010 m day^{-1}. The largest historical annual displacement of about 5 m was observed in 1997 (Weber and Hermann, 2000). The narrowing of the sloping path downstream is suspected to significantly impede the progression of the material, as underlined by the different direction of the displacement vectors (Fig. 2B).

Table 1
Point density of the TLS acquisitions in the local coordinate system and in the grid perpendicular to the viewing direction.

TLS acquisition	Local coordinate system		Grid	
	μ (pt m^{-2})	σ (pt m^{-2})	μ (pt $pixels^{-2}$)	σ (pt $pixels^{-2}$)
12 October 07	162.19	229.28	0.79	0.09
19 May 08	152.96	222.34	0.78	0.07
23 July 08	189.62	351.68	0.82	0.20
18 October 08	184.56	237.80	0.89	0.35
12 May 09	153.89	294.12	0.81	0.12
29 May 09	192.69	325.95	0.86	0.17
12 July 09	188.69	304.49	0.93	0.22
24 July 09	162.36	350.35	0.85	0.11
05 October 09	234.87	345.67	0.89	0.30
27 May 10	213.31	214.37	0.94	0.23

The confinement of the front due to the valley geometry, the free surface at the front and the possibility of sudden acceleration of the landslide can conduct to an obstruction of the stream. A sudden rupture or a fluidization of the front in a debris flow is a possible hazard scenario, as observed in other parts of the landslide (Malet et al., 2005). These reasons have motivated the start of monitoring campaigns of the front in order to characterize its local kinematics and detecting the presence of zones in extension or compression, and zones developing shearing (Fig. 1B).

3. TLS data collection

The monitoring was carried out with a long-range TLS Optech ILRIS-3D laser scanner which principle is based on the time-of-flight distance measurements using an infrared sensor (Slob and Hack, 2004). Mirrors inside the scanner allow the acquisition of a 40° wide and 40° high field of view in a single acquisition at a scanning rate of 2500 pt s^{-1} and an angular accuracy of 1.15×10^{-3}° and an angular divergence of 9.74×10^{-3}°. The range of the laser scanner is about 800 m in real field conditions. At each acquisition, the Cartesian coordinates of each target point are obtained with a normalized intensity value.

Ten acquisitions were realized from October 2007 to May 2010 from the same base station (positioning accuracy of ±0.5 m) at an average distance of 100 m from the landslide. At this distance, the footprint of the laser beam at the landslide ground surface is estimated at 0.04 m. Stable slopes formed of alternate gullies and crests around the landslide were systematically included in the scans (Fig. 1B) for the co-registration of the time series point clouds. As such rough terrains yield higher reliability in the co-registration, higher point density scans were systematically acquired to increase

Table 2
List of parameters and range of values used in the processing workflow at each processing steps.

Processing step	Processing task	Parameter	Range of values[a]
1. Pre-processing	Vegetation filtering	Grid spatial resolution	1.00 m
		Height above the grid	0.15 m
2. Coordinate transformation	Point-cloud orientation	*i*;*j*;*k*	*i* = [−0.965176; −0.261602; −0.000115] *j* = [0; 0; −1] *k* = [0.261482; −0.965208; −0.000517]
	Point-cloud scaling	*s*	7000
3. Displacement field calculation	Image-based correlation	Size of correlation window	30 × 30 pixels
		Size of explored window	150 × 150 pixels
		Correlation coefficient	>0.6
	Filtering	Amplitude threshold	12 m
		Upslope sliding direction	$Z_{final} > Z_{initial}$ (Z is elevation)
		Median filtering window	1 m × 1 m
4. Strain field calculation	Strain calculation	Strain window	3 m × 3 m

[a] The values used in this work are indicated as possible reference values for other applications.

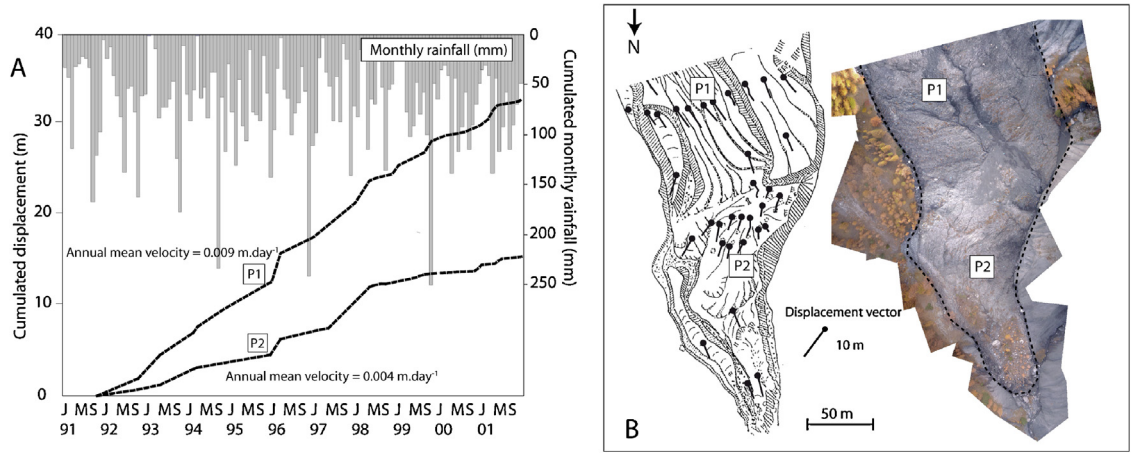

Fig. 2. Historical kinematics of the landslide toe. (A) Rainfall–displacement relationship between 1991 and 2001 for two positions at the toe (adapted form Malet, 2003). (B) Displacement vectors for the period 1996–2000 and aerial orthophotograph of 2008 showing the influence of the geometry of the stream valley on the sliding direction (adapted from Malet, 2003; Niethammer et al., 2012).

the topographic resolution (900.0–1148.3 pt m^{-2}) on these slopes. The short distance between the landslide and the stable slopes is an advantage for obtaining very accurate alignments. Only the last return pulse is registered to maximize the number of points reflected at the ground surface. The point clouds are constituted of 9–12 millions of points heterogeneously distributed on a topographic surface of ca. 16,000 m^2. The average point density at the ground surface varies from 153 pt m^{-2} to 235 pt m^{-2} for consecutive surveys with a maximum standard deviation of 351 pt m^{-2} and a maximal density of 1148 pt m^{-2} (Table 1 and Fig. 3).

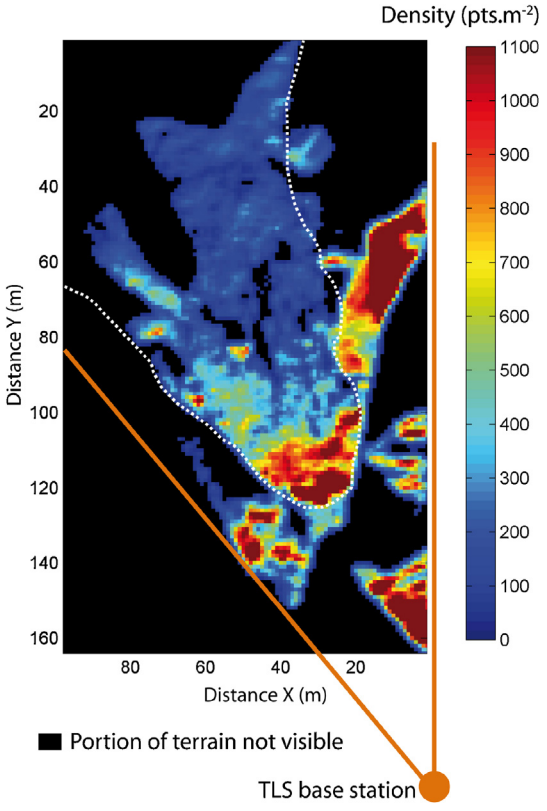

Fig. 3. Density of point cloud data in the horizontal plane (example of the acquisition of 24th July 2009). A point density value of 0 indicates portion of the terrain not visible from the TLS base station.

4. Data processing

The different steps in data processing (filtering and alignment of the point cloud time series, coordinate transformation, 3D surface matching, image cross-correlation) are detailed below. The parameters used in the processing steps of the workflow are summarized in Table 2.

4.1. Data pre-processing

4.1.1. Vegetation filtering and co-registration of the TLS point clouds

Although the laser beam is able to penetrate the canopy, numerous last return pulses originate from reflection on densely vegetated areas. These last return pulses on the vegetation are filtered with the method proposed by Prokop and Panholzer (2009). It consists in generating a low resolution DTM (spatial resolution of 0.5 m) from the point clouds. Because such DTM cannot reproduce local abrupt changes of slope morphology (typically induced by the presence of vegetation), it is used to identify points located at a vertical (Z direction) distance of ±0.15 m from the smoothed interpolated surface; these points are then removed from the original datasets. This technique allows filtering regions of sparse vegetation cover but is sensitive to the point cloud density. If the spatial resolution of the DTM is low, points on terrain steps and edges can be removed, while, if the spatial resolution is high, some parts of the vegetation cover are not filtered. Therefore, the filtering procedure is carried out iteratively by changing the spatial resolution of the DTM. For the Super-Sauze dataset, the filtering was carried put with the same parameters for all acquisitions. At the end, the technique allows a filtering of 90% of the vegetated points, while the other 10% were filtered manually.

The filtered point clouds are co-registered in a common local coordinate system by aligning one acquisition to one another using the stable slopes nearby the landslide which topography was preserved during the monitoring period (Figs. 1B and 4). These slopes can only be affected by shallow erosive processes (e.g. shallow slides of a few centimeter thick, small rockfalls of a few decimetric volume, incised gully-type water erosion) that can modify the ground surface. A small landslide occurring on these slopes can be easily identified visually in the point clouds or automatically by aligning all the stable surfaces together. If large artifacts (corresponding to a misfit greater than the defined range of error of 0.04 m) are identified, the points are removed from the dataset and

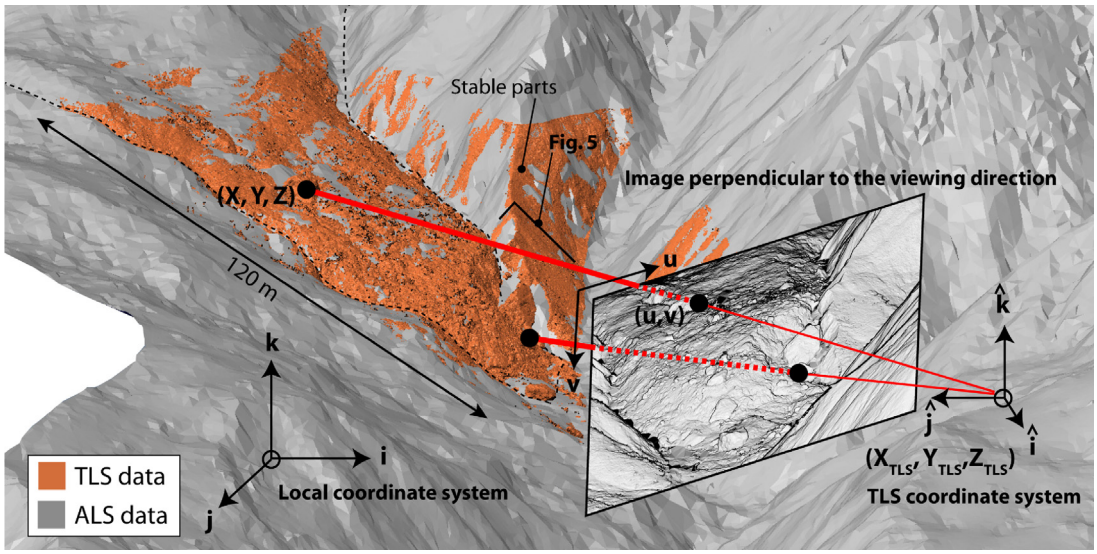

Fig. 4. Schematic presentation of the projective projection applied on the TLS point clouds with the different coordinate systems involved in the procedure. The alignment of the stable parts of TLS point clouds on the ALS point cloud is shown. The position of the profile extracted in Fig. 5 is also indicated.

the co-registration is iterated until the error is in the defined range. The ICP algorithm is used for the alignment and a 3D error of 0.04 m is calculated (Table 2 and Fig. 5).

The aligned point clouds are then transformed by point-to-point surface matching on the stable slopes identified in a georeferenced (e.g. French Lambert III coordinate system) Airborne Laser Scanning (ALS) point cloud of October 2007 (Fig. 4). The accuracy of the absolute alignment of the sequential point clouds is estimated to an average error of ~0.01 m and a standard deviation of ~0.14 m (Table 3). The point clouds filtering and alignment were processed with the software Polyworks 11.0 (InnovMetric, 2009).

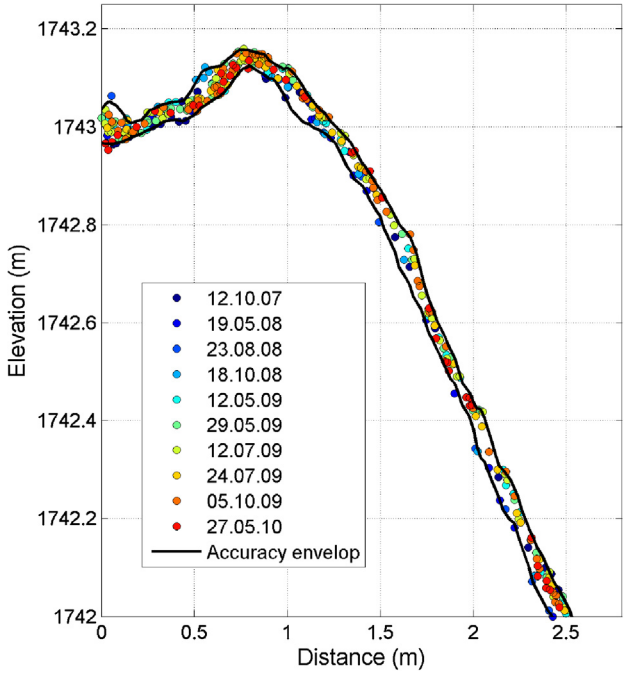

Fig. 5. Profile across the point clouds showing the co-registration quality. The location of the profile is indicated in Fig. 4.

4.1.2. Coordinate transformation and local 3D matching

Because the laser beam is generated from a punctual source, a projective transformation is used to represent the full 3D geometrical information in a plane perpendicular to the viewing direction of the TLS. This plane corresponds to the field of view selected by the operator on the liquid crystal display (LCD) of the scanner. This transformation allows a perfectly homogeneous distribution of the points in the plane. The relationship relating the 3D position (X, Y, Z) of each point to its position (u,v) in the plane is given by the collinearity equations (Kraus and Waldhäusl, 1994) These equations are based on the principle that each point is projected along a straight line crossing the projection center represented, for this work, by the average geographical position of the ten TLS surveys (X_{TLS}, Y_{TLS}, Z_{TLS}; Fig. 4):

$$u = s\frac{(\hat{\mathbf{i}}_{TLS}\bullet\hat{\mathbf{i}}_{Local})(X-X_{TLS})+(\hat{\mathbf{i}}_{TLS}\bullet\hat{\mathbf{j}}_{Local})(Y-Y_{TLS})+(\hat{\mathbf{i}}_{TLS}\bullet\hat{\mathbf{k}}_{Local})(Z-Z_{TLS})}{(\hat{\mathbf{k}}_{TLS}\bullet\hat{\mathbf{i}}_{Local})(X-X_{TLS})+(\hat{\mathbf{k}}_{TLS}\bullet\hat{\mathbf{j}}_{Local})(Y-Y_{TLS})+(\hat{\mathbf{k}}_{TLS}\bullet\hat{\mathbf{k}}_{Local})(Z-Z_{TLS})}$$
$$v = s\frac{(\hat{\mathbf{j}}_{TLS}\bullet\hat{\mathbf{i}}_{Local})(X-X_{TLS})+(\hat{\mathbf{j}}_{TLS}\bullet\hat{\mathbf{j}}_{Local})(Y-Y_{TLS})+(\hat{\mathbf{j}}_{TLS}\bullet\hat{\mathbf{k}}_{Local})(Z-Z_{TLS})}{(\hat{\mathbf{k}}_{TLS}\bullet\hat{\mathbf{i}}_{Local})(X-X_{TLS})+(\hat{\mathbf{k}}_{TLS}\bullet\hat{\mathbf{j}}_{Local})(Y-Y_{TLS})+(\hat{\mathbf{k}}_{TLS}\bullet\hat{\mathbf{k}}_{Local})(Z-Z_{TLS})} \quad (1)$$

where $\hat{\mathbf{i}}$, $\hat{\mathbf{j}}$ and $\hat{\mathbf{k}}$ are the unit vectors of the coordinate system of the TLS depending on its orientation in the local coordinate system, and $\mathbf{i}$, $\mathbf{j}$ and $\mathbf{k}$ are the unit vectors (1, 0, 0), (0, 1, 0), (0, 0, 1) of the local coordinate system. The symbol • corresponds to the scalar product of the unit vectors. The parameter s is the scaling factor used to define the grid resolution (in pixel), and which is determined in such a way that the average point density tends to 1 pt pixel^{-1} to

Table 3
3D geometrical errors expressed in average (μ) and standard deviation (σ) values. The co-registration errors are estimated relative to the TLS acquisition of 12 October 2007; the georeferencing errors are estimated relative to the ALS point cloud.

TLS acquisitions	Co-registration error		Georeferencing error	
	μ (m)	σ (m)	μ (m)	σ (m)
12 October 07	–	–	−0.004	0.13
19 May 08	0.002	0.032	0.001	0.14
23 July 08	−0.001	0.033	−0.013	0.14
18 October 08	−0.002	0.031	−0.008	0.14
12 May 09	0	0.029	−0.001	0.15
29 May 09	0	0.041	−0.012	0.15
12 July 09	0	0.032	−0.011	0.14
24 July 09	0.001	0.033	0.020	0.16
05 October 09	0	0.045	−0.060	0.14
27 May 10	−0.003	0.062	−0.020	0.15

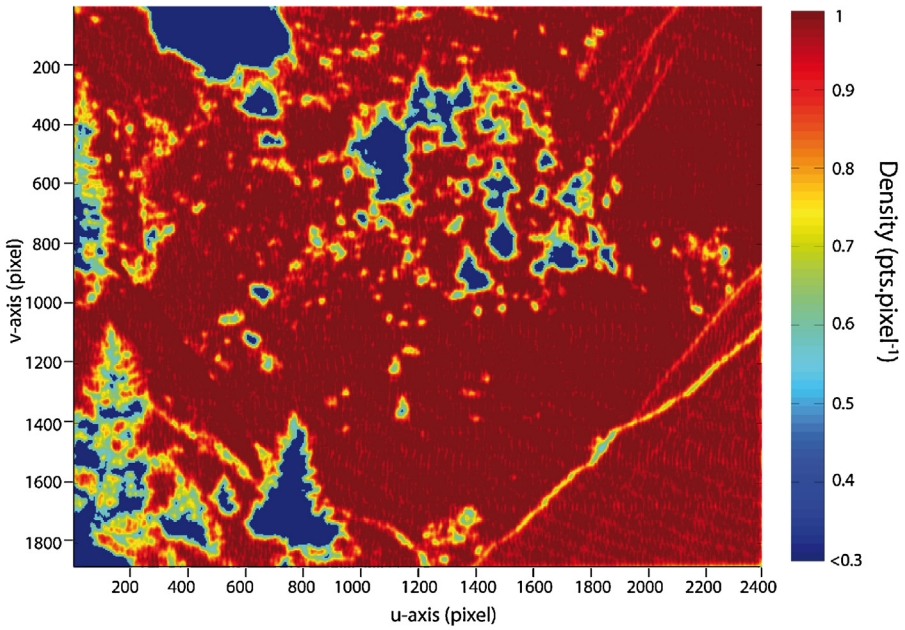

Fig. 6. Map presenting the point density in the plane perpendicular to the viewing direction of the laser scan and characterized by a homogeneous point distribution. The figure presents the acquisition of 24 July 2009. A point density value of 0 indicates portion of the terrain where vegetation is filtered.

minimize possible loss of information during the interpolation and exhaustively exploit all the geometrical information contained in the point clouds. A small value of s leads to a loss of accuracy in the displacement calculation because some points from the original point cloud will be projected and averaged in a unique pixel. At the opposite, a large value of s generates blank pixels without any information from the original point cloud. The influence of the interpolation algorithm will then be very important in the final results. Furthermore, the image size will be not optimized and the correlation computation will be more time consuming. The parameters s can be automatically determined using an iterative approach to get a point density projected in the image equal to one. In this study, a value of s corresponding to a grid size of 2400 × 1900 pixels was selected (Table 2).

Because the central projection described in Eq. (1) does not preserve distances between points, the area of terrain covered per pixel varies across the image. Therefore, the average pixel size is 1.8×10^{-3} m^2 with a standard deviation of 2.6×10^{-3} m^2. The same set of parameters has been used for every TLS survey in order to produce images with exactly the same geometry (e.g. viewing direction and sensor position).

Consequently, for all the time series, the average point density varies from 0.78 to 0.94 pt pixel^{-1} with a relatively low standard deviation of 0.18 pt pixel^{-1} (Fig. 6 and Table 1). In this case, the average point density is slightly lower than 1 pt pixel^{-1} because of the vegetation filtering in the original point clouds. The distance between the point clouds to the position of the laser scanner (X_{TLS}, Y_{TLS}, Z_{TLS}) is then determined and attributed for each pixel. For the pixels without any TLS information (e.g. pixels corresponding to filtered data), their value is linearly interpolated from the adjacent values. If a pixel contains more than one point, the average distance is attributed to the pixel. In theory, such situation cannot happen if the TLS surveys are systematically realized with the same acquisition parameters (scanner location, scanner orientation, acquisition resolution). These ideal conditions cannot be totally realized in the field because the TLS was installed on a tripod removed after each survey.

The type of representation of the topographical surface is important for the detection of the displacements. Because the correlation function gives good results when the input data contains regions of rapidly varying pixel information (Duffy and Hughes-Clarke, 2005), the norm of the 2D gradient in the u and v directions of the distance between the point clouds and the TLS base station is calculated to underline the morphology of the slope. The computed gradient values are then converted in gray-intensity value images (16 bits) (Schwalbe et al., 2008) and are used as inputs for the image correlation to compute the 2D displacement field in the plane perpendicular to the viewing direction of the TLS (Figs. 4 and 7).

4.2. Determination of the displacement field with a cross-correlation function

The determination of the displacement field is a two-steps procedure. First, the displacements are determined in the plane perpendicular to the viewing direction (2D displacement); second, the 2D displacements are converted in 3D displacements in the local reference system.

4.2.1. Determination of the displacement field in the plane perpendicular to the viewing direction

The 2D displacement fields in the plane perpendicular to the viewing direction are calculated with a 2D normalized cross-correlation function which is sensitive to the variation of gray-intensity values. The function is maximized to recognize identical intensity distribution patterns in a correlation window in two images in order to determine the displacement of the center of the correlation window. The function is defined in Eq. (2) (Chambon, 2003; Hild, 2003):

$$R_{d_1,d_2}(\Delta u, \Delta v) = \frac{\sum^{N_u}\sum^{N_v}(\boldsymbol{d_1}(u,v) - \bar{d}_1)(\boldsymbol{d_2}(u+\Delta u, v+\Delta v) - \bar{d}_2)}{\sqrt{\sum^{N_u}\sum^{N_v}(\boldsymbol{d_1}(u,v) - \bar{d}_1)^2}\sqrt{\sum^{N_u}\sum^{N_v}(\boldsymbol{d_2}(u+\Delta u, v+\Delta v) - \bar{d}_2)^2}} \quad (2)$$

where R_{d_1,d_2} is the coefficient value that is maximized, $(\Delta u, \Delta v)$ is the corresponding displacement along the u-axis and v-axis, $\boldsymbol{d_1}$

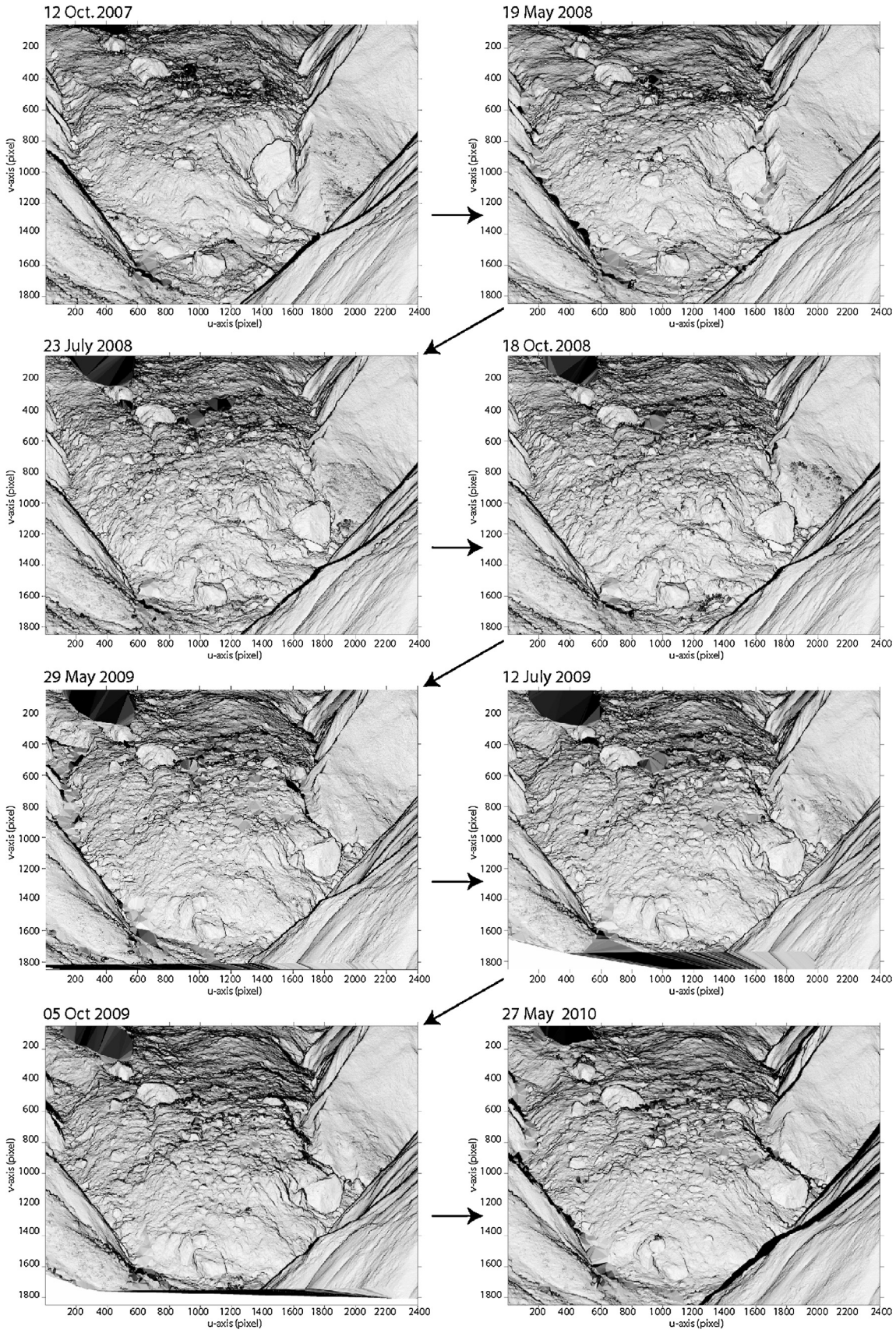

Fig. 7. Images derived from the gradient calculation on the TLS point cloud time series. The morphology of the slope is very well represented and the progression of the landslide is also highlighted. These gray-scale images are then correlated.

Table 4
Statistical differences between the imposed displacements and the computed displacements.

Short imposed displacement (m)	$\Delta X = 0.6 \times 10^{-2}$	$\Delta Y = 1.8 \times 10^{-2}$	$\Delta Z = -0.7 \times 10^{-2}$	$\Delta Total = 2.0 \times 10^{-2}$
Mean error (m)	0.3×10^{-2}	-0.4×10^{-2}	0.4×10^{-2}	0.6×10^{-2}
Median (m)	0	0	0	0
Standard deviation (m)	1.7×10^{-2}	2.7×10^{-2}	1.5×10^{-2}	1.5×10^{-2}
Maximum (m)	16.8×10^{-2}	12.4×10^{-2}	14.8×10^{-2}	9.9×10^{-2}
Minimum (m)	-18.5×10^{-2}	-18.9×10^{-3}	-7.4×10^{-2}	-0.9×10^{-2}
Large imposed displacement (m)	**$\Delta X = -0.320$**	**$\Delta Y = 0.887$**	**$\Delta Z = -0.334$**	**$\Delta Total = 1$**
Mean error (m)	-0.6×10^{-2}	0.7×10^{-2}	-0.8×10^{-2}	0.9×10^{-2}
Median (m)	0	0	0	0
Standard deviation (m)	2.6×10^{-2}	2.9×10^{-2}	2.2×10^{-2}	2.7×10^{-2}
Maximum (m)	16.6×10^{-2}	19.7×10^{-2}	16.3×10^{-2}	10.0×10^{-2}
Minimum (m)	-17.8×10^{-2}	-19.9×10^{-2}	-17.6×10^{-2}	9.0×10^{-2}

and $\boldsymbol{d_2}$ are the correlation windows in, respectively, the reference and the interrogation images containing the gray-intensity values, N_u and N_v are the dimensions of the correlation windows along the u-axis and v-axis, and $\bar{d}_1$ and $\bar{d}_2$ correspond to the spatial average of $\boldsymbol{d_1}$ and $\boldsymbol{d_2}$, respectively.

A correlation algorithm where the displacement field is determined in the Fourier domain is used (Chambon, 2003). In practice, a correlation window $\boldsymbol{d_1}$ is defined in the reference image (Fig. 8) and the corresponding correlation window $\boldsymbol{d_2}$ is searched in an explored area (defined by the parameters W_u and W_v, respectively along the u-axis and the v-axis) of the interrogation image. The process is repeated for each pixel of the reference image by shifting the explored area in both directions of the interrogation image (Fig. 8). The Euclidian distance (Δu, Δv) between the center of the correlation window and the position of the maximum correlation coefficient value R_{d_1,d_2} in the interrogation image corresponds to the displacement magnitude. If neither deformation nor rotation develops at the scale of the correlation window, the value of correlation coefficient tends to one.

The size of the correlation window is a compromise between the requested measurement accuracy and the amplitude of the displacement (Delacourt et al., 2007). An increase in size of the correlation window takes into account a higher point density and ensures a good signal-to-noise ratio, but the accuracy can decrease since the displacements are computed on a larger ground surface. A small correlation window makes the correlation computations more sensitive to noise and can render inaccurate displacement estimates. The optimum correlation window size is chosen iteratively by applying a trial and error procedure. In this work, a correlation window of 30 pixels ($N_u = N_v = 30$) produced the most uniform vector fields; this correlation window corresponds to a ground surface size varying between 0.5 m^2 and 3.5 m^2. The calculated displacement field is sensitive to the parameters of the image correlation algorithm (e.g. size of the correlation window, image texture) which are discussed in Travelletti et al. (2012).

The size of the explored area is defined according to expert knowledge of the landslide kinematics or, simply, by estimating visually the maximum displacement on two gray-intensity value images. To ensure that the maximum displacement can be detected, the size of the explored area is fixed at three times the amplitude of the maximum expected displacement. In this work, an explored area of 150 pixels ($W_u = W_v = 150$) is selected.

A sub-pixel correlation is then used to detect displacements magnitudes below the pixel size in the image. The sub-pixel displacement is computed after the pixel-level correlation. An iterative procedure is used to identify the maximum of the correlation function interpolated with a bi-parabolic spline and with a maximization procedure based on the simplex method (Press et al., 1997; Chambon, 2003). The result of the correlation corresponds to the displacements Δu and Δv along, respectively, the u- and v-axes. The value of correlation defines the quality of matching. Fig. 9 presents the results of the correlation in the image plane.

4.2.2. Reconstruction of the 3D displacement field

Because the pixel sizes vary in the images, the displacement fields correlated in the image plane cannot be directly interpreted in terms of absolute metric displacements. Therefore an orthorectification procedure is applied to reconstruct the 3D displacement field. Three grids of coordinates X, Y, Z are generated using Eq. (1) with the same parameter s and unit vectors used to create the gray-intensity images. Consequently the grids of coordinates have exactly the same geometry as the gray-intensity images. After the determination of the 2D displacements in the gray-intensity image (Fig. 9), a bi-linear interpolation is used to associate the triplet of coordinates (X, Y, Z) obtained from TLS surveys to each initial (u, v) and final ($u + \Delta u$, $v + \Delta v$) positions of the displacement vectors in the images. This procedure is similar to the backward projection technique used in photogrammetry (Corripio, 2004; Travelletti et al., 2012). Finally the incremental displacements ΔX, ΔY and ΔZ in the local coordinate system are calculated.

4.2.3. Accuracy of the processing routine

To evaluate the accuracy of the processing routine without considering any external sources of error (e.g. instrumental errors, low ground reflectivity, large ground deformation, co-registration errors), synthetic homogeneous displacements were applied in the TLS point cloud of May 2008. A correlation window of 30 pixels was selected. The difference of the imposed displacements with the calculated displacements (ΔX, ΔY and ΔZ and the total displacement) is used to evaluate the error. The accuracy depends on the gradient contrast and on the accuracy of the normalized cross-correlation function. Two tests were realized to quantify the robustness of the approach to measure, respectively, large and small displacements; in the first case, the test consisted in applying a rigid translation of one meter in the main sliding direction ($\Delta X = -0.34$ m, $\Delta Y = 0.88$ m, $\Delta Z = -0.33$ m), in the second case, the test consisted in applying a rigid translation in the main sliding direction with a magnitude in the range of the TLS accuracy of 0.02 m ($\Delta X = -0.6 \times 10^{-2}$ m, $\Delta Y = 1.7 \times 10^{-2}$ m and $\Delta Z = -0.7 \times 10^{-2}$ m). The results are summarized in Table 4.

The errors are estimated by the average and the standard deviation of the differences between the synthetic homogeneous displacement imposed in the TLS point clouds and the displacement computed with the processing routine. For both the large and the small displacements, the 3D displacements in the local coordinate system are well estimated, with an average error of less than 0.01 m with a standard deviation of 0.02 m. The correlation algorithm succeeds in recovering small displacement for more than 50% of the points (median value equal to 0).

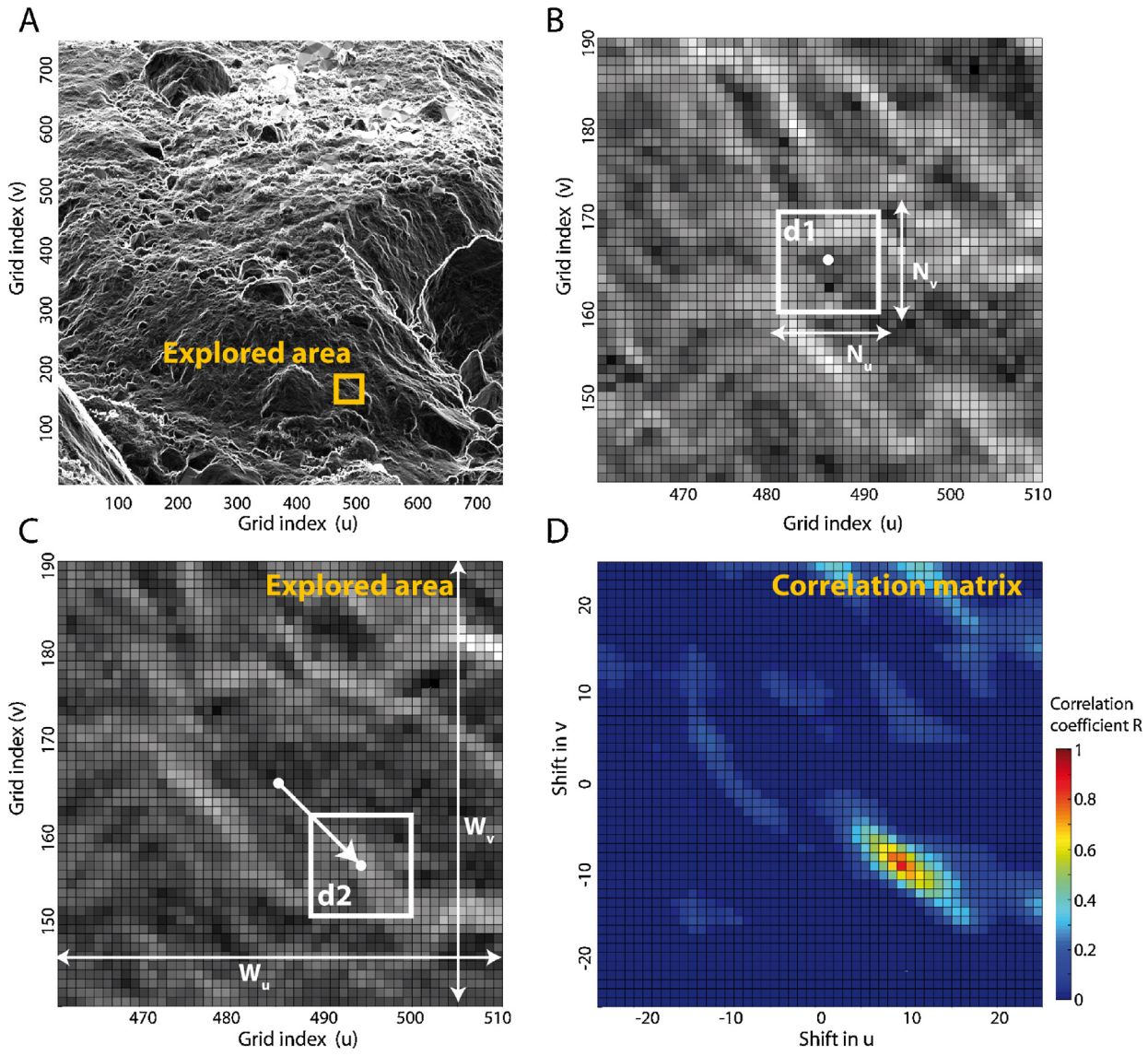

Fig. 8. Principle of the image correlation. (A) Gray-intensity value of the interrogation image and location of the explored area, (B) correlation window d1 of the reference image. N_u and N_v are the size of the correlation window, (C) explored area of size W_u and W_n of the interrogation image. The correlation window d2 is shifted in the directions u and v in the explored area, the correlation coefficient R between d1 and d2 is calculated for each grid shift. The location of the maximum correlation coefficient is a direct measurement of the displacement (white arrow) with respect to the origin of the correlation window d1, (D) values of the correlation coefficient R calculated for each grid shift.

4.2.4. Filtering of the computed displacement fields

As image correlation is a statistical technique (e.g. the more the correlation coefficient is close to one, the higher is the probability that the object found in the interrogation image is the searched one), it can always provide a solution, but which is not systematically accurate. The low correlation coefficient values are caused by important deformation or rotation of the tracked object in the interrogation image. Therefore filtering is used in order to remove the outlier values of computed displacements. The filters are based on:

- the value of the correlation coefficients: loss of coherence can occur during the calculations because of possible important changes in surface states between the reference and the interrogation images. Therefore, a threshold value of $r = 0.6$ is used to remove the badly correlated points. However, the value of the correlation is not a sufficiently discriminating criterion because some pixels can display high correlation values even if they do not represent the same object (for instance two trees or two large boulders having the same geometry; Casson et al., 2005);
- the value of the displacement amplitude and direction: pixels characterized by an upslope sliding direction or by a large displacement amplitude (e.g. superior to the average or superior to five times the standard deviation) with reference to a priori knowledge on the kinematics are filtered Debella-Gilo and Kaab, 2011; Travelletti et al., 2012).

Further, a median filter is used to reduce the noise in the three grids of displacement components (ΔX, ΔY, ΔZ). The displacement values of each pixel are replaced by the statistical median of the neighboring entries. A median filter is relevant at preserving the sharp high-frequency details whilst also eliminating noise represented by isolated and incoherent displacement (direction and amplitude) relative to the neighborhood ("speckles"). Finally, median filtering allows obtaining smooth transitions in the displacement field which are necessary conditions for the strain calculation (Pan et al., 2009).

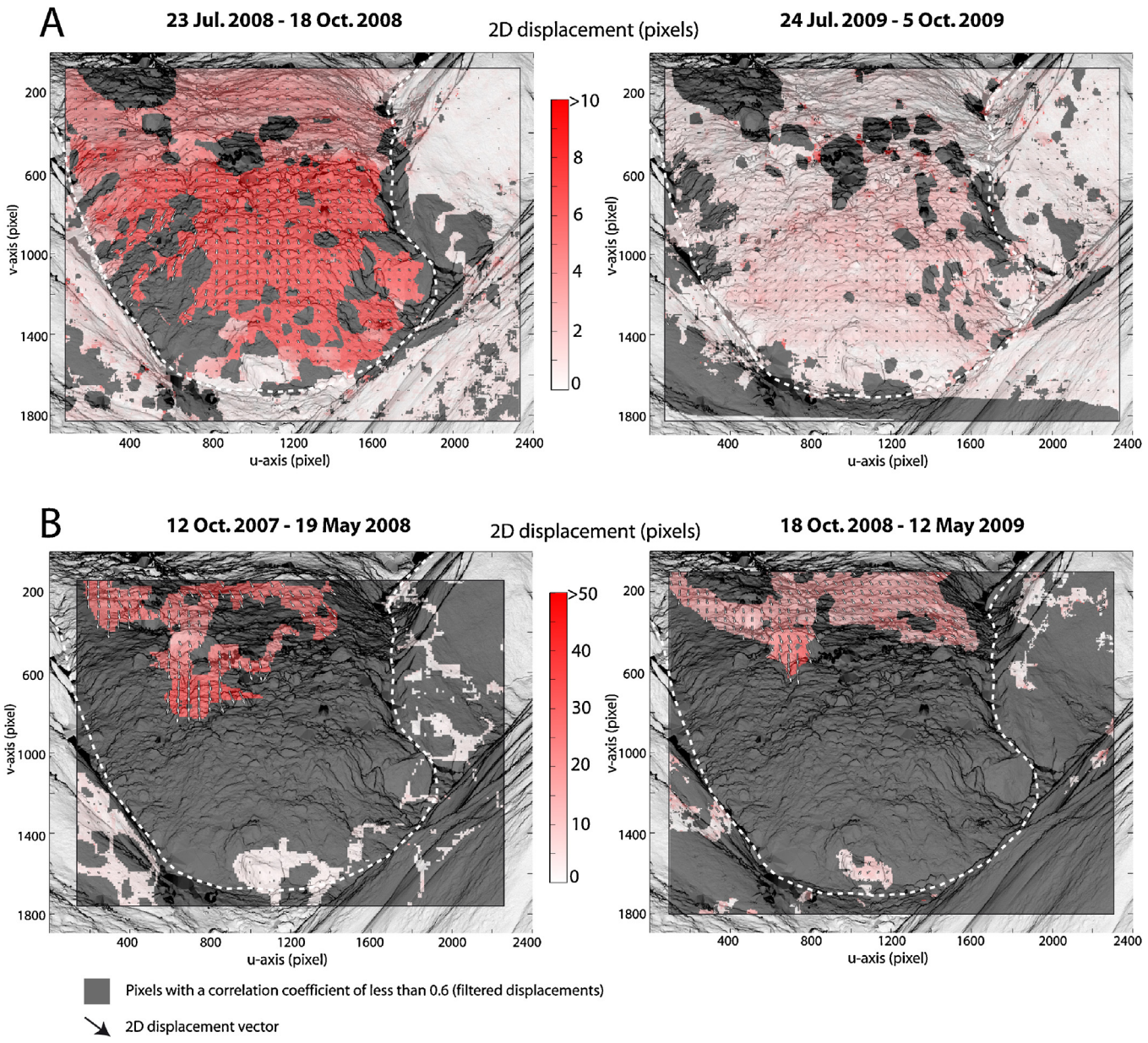

Fig. 9. 2D displacement fields obtained from the correlation of the gray-intensity images related to the acquisition periods of (A) July–October of the years 2008 and 2009, and (B) October–May of the years 2007 and 2008. The displacement maps are draped on their corresponding gray-intensity images.

4.3. Determination of the strain field

The strain fields are determined from the computed displacement fields in order to characterize possible strain localization and the material behavior in the damaging zone. Because the displacements are mainly in the horizontal plane, the strain fields are determined with the 2D Cauchy strain tensor E (Eq. (3); Teza et al., 2008; Pollard and Fletcher, 2010):

$$E = \begin{bmatrix} \dfrac{du_x}{dx} & \dfrac{1}{2}\left(\dfrac{du_x}{dx} + \dfrac{du_y}{dy}\right) \\ \dfrac{1}{2}\left(\dfrac{du_x}{dx} + \dfrac{dv_y}{dy}\right) & \dfrac{dv_y}{dy} \end{bmatrix} \quad (3)$$

where u and v refer to the incremental displacement along the x- and y- direction in the local coordinate system ($u = \Delta X$, $v = \Delta Y$). A local least square fitting technique is used to compute the 2D strain tensor at each location of the grid (Pan et al., 2009). A strain window of $(2m+1)^*(2m+1)$ is defined. If the strain window is small enough, the distribution of the displacement components can be estimated as a linear plane (Pan et al., 2009). Eq. (4) is then solved for each grid cell and for the two components u and v:

$$\begin{aligned} u(i,j) &= a_1 x + b_1 y + c_1 \\ v(i,j) &= a_2 x + b_2 y + c_2 \end{aligned} \quad (4)$$

where i, j are the coordinates in the strain window; $u(i,j)$ and $v(i,j)$ are the displacement components at the location (i,j); a_1, b_1, a_2, b_2 are the displacement gradients to be determined and c_1 and c_2 are constant values (which are canceled in the differentiation of the displacement components for the strain tensor estimation). This overdetermined system of equations is then formulated in its

matrix form and is solved in a least-squares sense. To find the value of the unknowns a_1, b_1 and c_1, Eq. (3) becomes Eq. (5):

$$\begin{bmatrix} 1 & -m & \\ 1 & -m+1 & \\ \vdots & \vdots & \vdots \\ 1 & 0 & 0 \\ \vdots & \vdots & \vdots \\ 1 & m-1 & m \\ 1 & m & m \end{bmatrix} \begin{bmatrix} a_1 \\ b_1 \\ c_1 \end{bmatrix} = \begin{bmatrix} u(-m,-m) \\ u(-m+1,-m) \\ \vdots \\ u(0,0) \\ \vdots \\ u(m-1,m) \\ u(m,m) \end{bmatrix} \quad (5)$$

where $m \in \mathrm{N}|^*$.

The procedure is similar to find the values of the unknowns a_2, b_2 and c_2. The components of the Cauchy strain tensor are then estimated with $a_1 = \frac{du_x}{dx}$, $b_1 = \frac{du_x}{dy}$, $a_2 = \frac{dv_x}{dx}$ and $b_2 = \frac{dv_x}{dy}$. As the regular grids display a homogenous distribution of displacements, the least-squares fitting is not influenced by important difference of points density in the strain window, thus making the gradient estimations more robust.

Because the strain tensor E is real and symmetric, the two eigenvalues e_1 and e_2 are computed and correspond to the change of length per unit of length in the direction having the maximum and minimum extension The computed deformation field corresponds to the surface strain field (defined as $\varepsilon_S = e_1 + e_2$; positive for extension) and the shear strain field (defined as $\gamma = |e_1 - e_2|$). A large strain window leads to smooth strain fields useful to depict deformation at large scales. A small strain window leads to more accurate strain field useful to depict deformation at small scales; however, at such scales, the results are also more sensitive to noise. In this study, taking into account the size of the landslide toe (50 m × 100 m), a strain window of 3 × 3 pixels ($m = 1$ for a grid mesh size of 1 m) is used.

5. Results: displacement and deformation analysis of the landslide front

5.1. Displacement pattern

The displacements are well reproduced for all acquisition periods. The contrast in the displacement values between the landslide and the surrounding stable slopes gives confidence in the calculated displacement field. Four acquisitions periods (October 2007–May 2008, July 2008–October 2008, October 2008–May 2009, July 2009–October 2009) are presented (Fig. 10A and B).

The slope deformations at the scale of the correlation window are sufficiently low in the periods characterized with a slow displacement rate to obtain high correlation coefficients, especially between the months of July and October (Fig. 10A). For the period July 2008–October 2008, displacements between 0.5 and 1.5 m are observed, corresponding to an average displacement rate of 0.06–0.17 m day^{-1}. The displacement field exhibits significant spatial variability. The largest displacements are detected at the front where the slope gradient increases. The detachment of a small compartment is also highlighted. During the same period of the following year (July 2009–October 2009), a very different kinematics is observed both in terms of magnitude and spatial distribution. Displacements are shorter and range from 0.1 m at the front of the landslide toe to 0.6 m in the upper part, thus corresponding to an average displacement rate of 0.001–0.008 m day^{-1}.

The ground surface morphology between October and May of 2008 and 2009 is affected by strong deformation. No coherent displacement vectors can be obtained in the lower part of the front due to excessive ground deformation at the scale of the correlation window. Consequently, the values of correlation coefficient are low (<0.6) and the calculated displacements were filtered. According to the criteria detailed in Section 4.2.4, 30% to 40% of the total number of pixels are not filtered (Fig. 10B). The upper part of the front exhibits lower deformation at the scale of the correlation window. Therefore the values of correlation coefficient are higher and the displacements are reliable. This area displays a uniform displacement field showing that this part of the front behaves like a rigid body.

5.2. Validation of the computed displacements

Two methods are used to validate the computed displacements: (i) the first method consists in comparing the obtained displacements with the displacements derived from the ICP method following the procedure described in Oppikofer et al. (2009); (ii) the second method consists in comparing the obtained displacements with differential GPS surveys (dGPS) of blocks (horizontal and vertical accuracy of 0.02 m and 0.05 m). The dGPS measurements were acquired in real time kinematic (RTK) mode using a fixed reference station located at a distance of 250 m from the landslide. Marks were painted on the blocks to be measured with an error of ca. 1 cm.

Comparison with the ICP method allows evaluating the accuracy by taking into account the noise in the data (e.g. instrumental error, material reflectivity, incidence angle). The effects of co-registration errors on the displacement estimates are thus not considered. Five rigid blocks distributed on the landslide are identified in the point clouds for each TLS acquisition (Fig. 11A). The blocs are triangulated in the plane normal to the laser viewing direction in order to minimize the effect of shadow zones in the interpolation. The triangulated blocks of the first TLS acquisition are aligned on their corresponding triangulated blocks in the second TLS acquisition. The comparison of the displacements is performed exactly in the part of the blocks where a displacement obtained by the correlation is located assuming a distance tolerance of 0.30 m. The rapid convergence of the ICP algorithm gives good confidence in the displacement computations. The accuracy of the ICP method is evaluated by calculating the residual misfit of the block alignments. An average error of 0.01 m and a standard deviation of 0.01 m is obtained. The results of the comparisons between the displacement obtained with the ICP method and those derived form the correlation are synthesized in Fig. 10B. The displacements obtained from both methods are in very good agreement ($r^2 = 0.99$) with an average error and a standard deviation of 0.004 m and 0.025 m, respectively.

The comparison with the dGPS observations allows one to evaluate the accuracy of the approach by taking into account the noise in the TLS data and the co-registration errors. The displacements perfectly correlate ($r^2 = 0.99$). An average error and a standard deviation of 0.008 m and 0.04 m are respectively determined (Fig. 11C). Consequently, the whole error budget of the workflow is mainly due to the co-registering error of the point clouds. Actually the displacements measured with the dGPS are exactly of the same order as the error of co-registration (about 4 cm; Fig. 4).

5.3. Strain analysis

The strain field derived from the acquisition periods of July–October 2008 and 2009 is used to illustrate the kinematics of the toe. The first step consists in determining the accuracy of the computed strain field. A null hypothesis test is applied on the stable slopes assuming that the strain error in these parts is similar to the strain error in the landslide. This hypothesis is motivated by the fact that no deformation should occur on the stable parts of the landslide. If a deformation is calculated, it means that the computed displacement value is noise. Actually the strain calculation is very

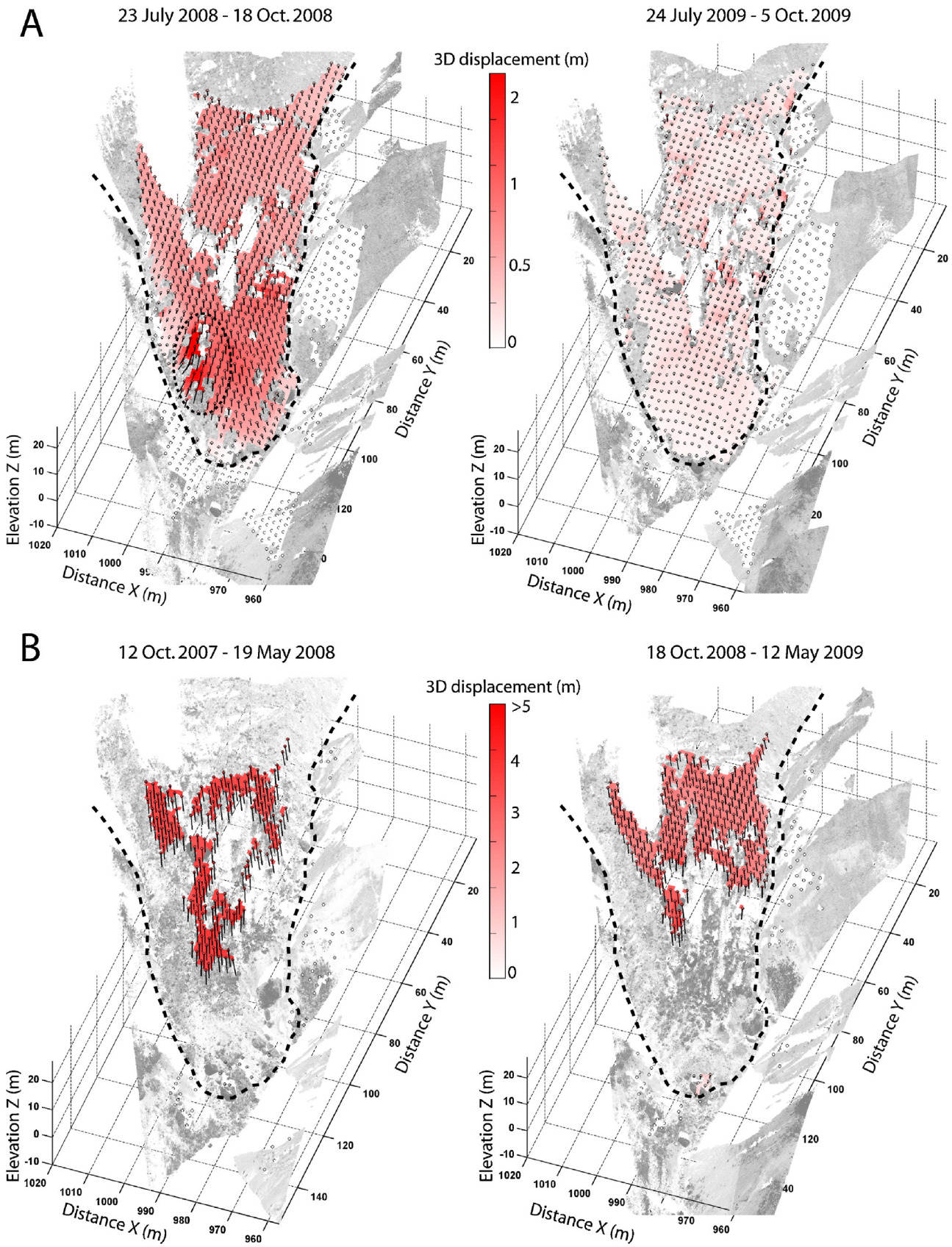

Fig. 10. 3D displacement fields obtained by point cloud time series for the acquisition periods of (A) July–October of the years 2008 and 2009, and (B) of October–May of the years 2007 and 2008. The dashed circle indicates the detachment of some material at the front. The displacement maps are draped on their corresponding point clouds (intensity values).

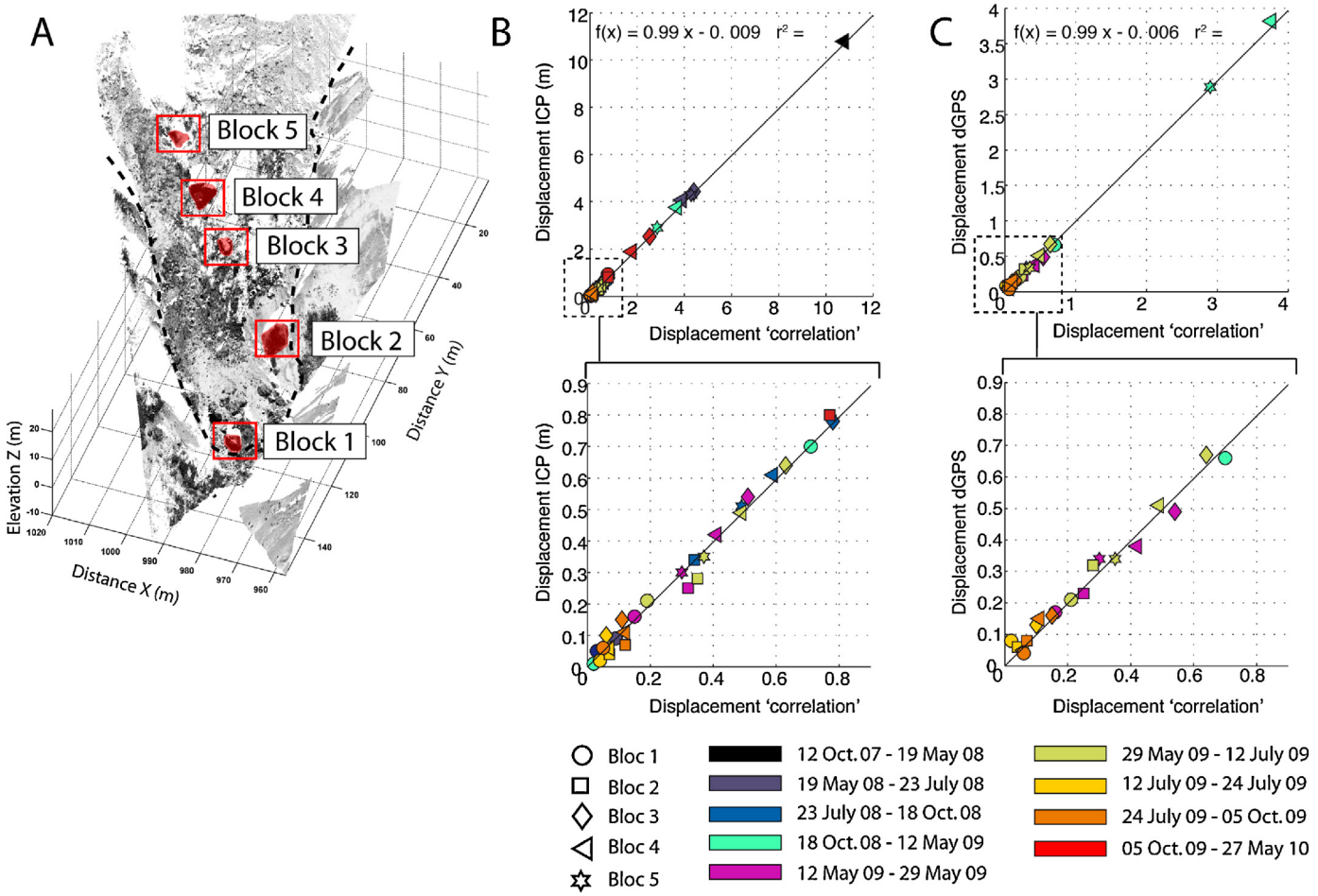

Fig. 11. Comparison of the displacement values obtained by correlation to the values estimated with the ICP method and with dGPS monitoring. (A) Location of the blocks in the point cloud. (B) Comparison with the ICP method. (C) Comparison with repeated dGPS surveys.

sensitive in displacement variations as it is its first derivative (see Eq. (3)). This justifies the necessity to filter the displacement field before the strain calculation. Therefore analysing the strain values on the stable part is a good indicator to estimate the sensitivity of the strain computation to noise. In this study, the accuracy analysis on the stable slopes shows that more than 90% of the surface strain and shear strain ranges between $\pm 2 \times 10^{-3}$ which is considered as the lowest interpretable value. The importance of the compression and shear strain affecting the front explains why the correlation computation sometimes tends to fail in that part of the landslide (Fig. 11A and B).

The strain analysis allows discriminating mechanical units in extension, compression and affected by shearing (Fig. 12). Note that because of the finite size of the correlation and strain windows, a significant smoothing of the strain fields is introduced associated to a spatial spreading of the structures. The upper part of the front is characterized by a succession of approximately parallel bands (width of 5–10 m) in compression and extension whose main orientation is perpendicular to the sliding direction (Fig. 12A). Except near the landslide boundary, the upper part is not affected by important shearing (Fig. 12B).

The location of the compression and extension zone changes from 2008 to 2009, thus suggesting a possible displacement of these areas downslope.

In 2008, extension is observed, thus inducing compression in the material located in the lower part of the front (Fig. 12A). The consequence of this extension results in the development of tensile fissures identifiable in the field (Fig. 13). The front is also affected by important shearing concentrated along the landslide boundary. The high shear values in these areas are confirmed by very persistent shear fissures affecting the landslide material (Fig. 13).

In 2009, the deformation affecting the front is less important than in the previous year; the displacements in that part are lower and more spatially uniform.

6. Discussion

In the case of objects scanned from a single position, the simplification of the 3D matching problem to a 2D matching problem is possible without significant loss of information during the processing chain due to an optimized grid selection according to the point density.

6.1. Advantages and limitations of the proposed methodology

The proposed workflow has many advantages for TLS investigation of landslides. First, the approach exploits all the potential of the high sampling density acquired with TLS instruments. Second, 3D displacements are derived from the correlation in opposition to the 1D displacement obtained classically from DEM differencing (Bitelli et al., 2004). The displacements can therefore be used for strain computations allowing a more exhaustive analysis of the landslide kinematics. Third, the quality of displacement estimation can be expressed through the value of the correlation coefficient R_{d_1,d_2} (Eq. (2)).

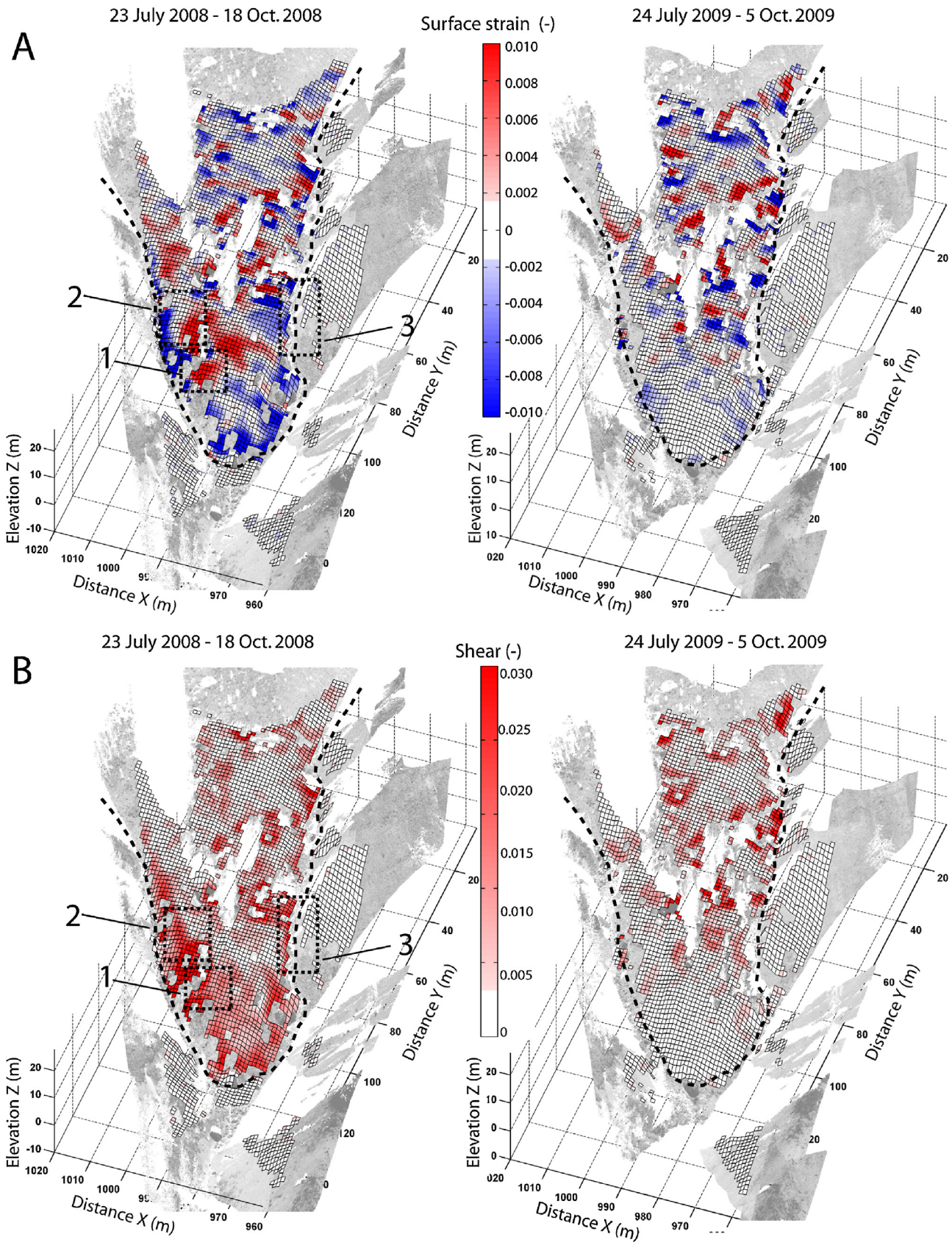

Fig. 12. Strain fields obtained by TLS measurements for the acquisition periods of July–October of the years 2008 and 2009. (A) Maps of the surface strain (a positive value means extension). (B) Maps of the shear strain. The dashed squares refer to Fig. 11. The strain maps are draped on their corresponding point clouds (intensity values).

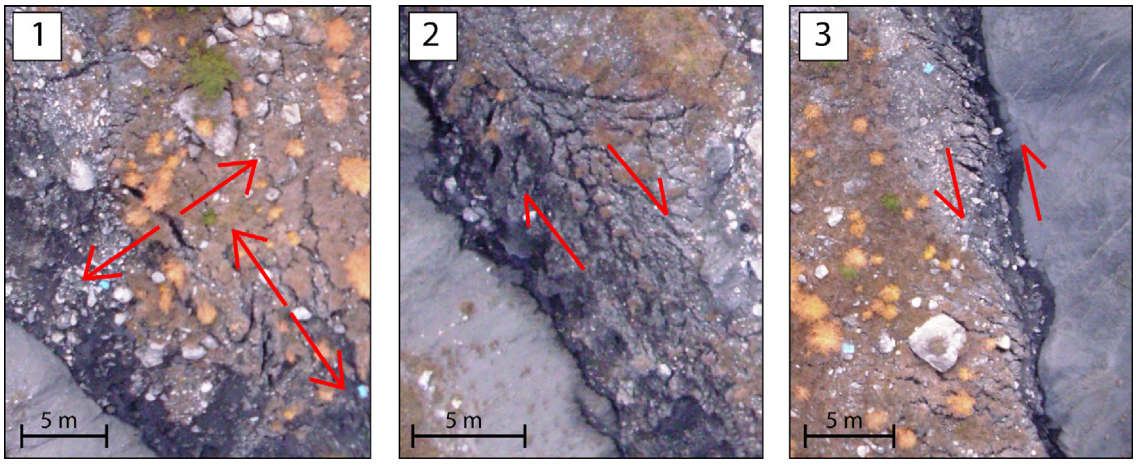

Fig. 13. Tensile fissures (1) and shear fissures (2 and 3) observed at the front on an orthophotograph acquired in October 2008 by Niethammer et al. (2010). The location of the pictures is indicated in Fig. 12.

Because the points clouds are back projected in the acquisition geometry (in a plane perpendicular to the viewing direction), the shadow zones are not visible in the image plane. In that strict sense, the presence of shadow is minimized. Thus, the displacement calculations are not affected by areas in the image plane without any information (typically in shadow zone if the same scene would be represented in the 3D space). If shadow areas are still present, the influence of the interpolation algorithm on the results would be important, because a 3D position had to be attributed to each pixel. In the proposed workflow, the influence of the interpolation algorithm is practically null since each pixel of the image contains exactly one 3D point (all the points are homogenously distributed in the image), except in the areas where the vegetation was filtered. Consequently the geometrical information contained in the original point clouds is not lost.

However, the results are limited by factors related to the field conditions, the TLS data processing and the 2D correlation technique. The amplitude of deformation rate between two TLS acquisitions is the most critical factor that affects the quality of the correlation. A conservation of the ground surface morphology is essential for reliable displacement measurements, which is also a prerequisite in most 3D matching algorithms (Teza et al., 2007). Unfiltered vegetation is also an important factor that influences the quality of the displacement estimates. Nevertheless, in certain circumstances, rigid parts of the vegetation (e.g. tree stumps) can be useful if there are perfectly recognizable in consecutive TLS acquisitions. They can enhance the texture of the 2D images perpendicular to the viewing direction, thus better constraining the 2D correlation computations. Instrumental and co-registration errors are the major factors affecting the accuracy of the displacements (Monserrat and Crosetto, 2008). Independently of the factors previously cited (which affect also the accuracy of classical 3D matching algorithms), the 3D simplification problem implies some limitations inherent to the simple 2D correlation algorithm used in this study. A first limitation is that simple 2D correlation techniques cannot track objects that are affected by very important rotation between two consecutive acquisitions (Lewis, 1995). Correlation techniques based on polar mappings (Nagashima et al., 2007) or edge image correlation (Liu, 2008) dealing with rotation problems can be also implemented in the proposed workflow. However, regarding the error on the displacement obtained in this study (4 cm) and the amplitude of displacements, the use of a simple correlation approach is very well adapted. A second limitation is linked to the use of a perspective projection. The consequence is that the distances and the angles are not preserved in the 2D images. If an object moves considerably from the background to the foreground of the image, it will be affected by an important perspective distortion that classical correlation algorithms cannot manage. This problem can be solved by using correlation algorithms allowing iterative deformation of the correlation window (Raffel et al., 2007). Lowly textured surface is also another factor that impedes reliable 2D correlation (Travelletti et al., 2012).

Finally, more complex image correlation methods exist with the advantage of minimizing the number of parameters to be selected by the operators. Such sophisticated multi-scale and hierarchical image correlation methods (e.g. Mic-Mac for instance; Deseilligny et al., 2013) allows to automatically select the optimal parameters.

6.2. Geomorphological and hydro-mechanical evidences of the landslide behavior

The long-term displacement magnitudes are directly correlated with the slope hydrology, and more specifically with the changes in pore water pressure which are continuously measured in a piezometer located at 80 m from the ultimate lobe of the landslide (Fig. 14). The important displacements (block 4; Fig. 9) observed between May 2007 and October 2008 (e.g. 14.7 m) is related to an increase of pore water pressure of about 15 kPa. After the peak of pore water pressure observed on the 15 April 2008, the general decrease of pore water pressures due to the drainage of the landslide aquifer controls the decrease of displacement rate (e.g. average displacement rate of 0.027 m day^{-1}) in the summer period. Transient increase of pore water pressure are observed but their influences on the landslide kinematics are not perceptible due to the large time span between the TLS acquisition. As expected, the front acceleration between October 2008 and May 2009 is directly correlated with a recharge of the landslide aquifer and consequently an increase of the pore water pressure. The lower magnitude of pore water increase (10 kPa) than in 2008 results directly in lower displacement magnitudes (e.g. 4.6 m). An average displacement rate of 0.002 m day^{-1} is estimated in summer.

Some questions arise about the succession of compression and extension zones observed in the upper part of the front by the strain analysis (Fig. 12). Actually Savage and Smith (1986) and Picarelli et al. (2005) demonstrated that slow-moving landslides affected by internal deformation can present such features. Positive excess pore water pressures under initially undrained conditions can be generated in these areas.

This mechanism is susceptible to trigger a fluidization of the front if the stresses are applied over very short time and if the

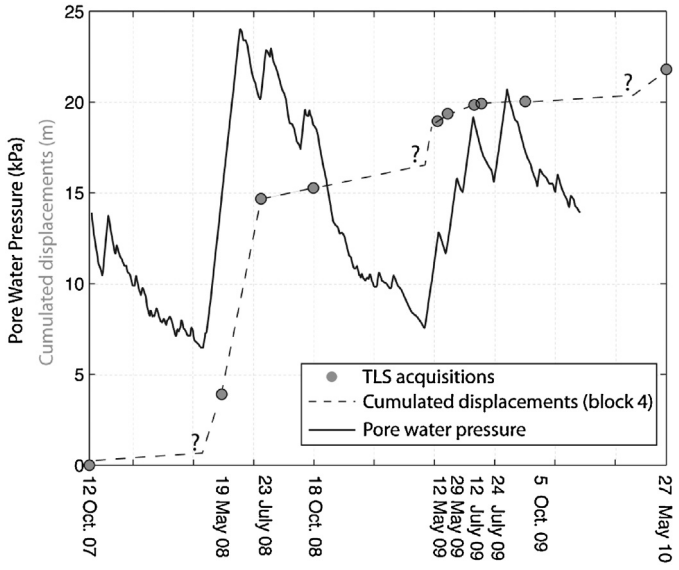

Fig. 14. Relationship between pore water pressure and cumulated displacements of the landslide front during the TLS monitoring period. The date of the acceleration initiation in the spring season is unknown and is therefore assumed to be close to the date corresponding to the onset of rising pore water pressures.

hydraulic permeability of the material is very low. This mechanism was also illustrated by van Asch et al. (2006) who suspected that, in certain cases, excess pore pressures can develop due to compression and extension zones in a moving body due to changes in slope gradient or in the bedrock geometry. van Asch et al. (2006) also showed by numerical modeling that liquefaction is possible in the remolded clays of the Super-Sauze landslide. The energy will not dissipate through friction inside the landslide material, but can be transformed into kinetic energy and initiate liquefaction. These considerations point out the utility of monitoring the evolution of the strain field at high spatial resolution to localize possible areas accumulating strains which are susceptible to liquefy in case of rapid loading.

7. Conclusion

This work presents a simple approach to estimate the 3D displacement fields from TLS point cloud time series using an image-based correlation approach and fully exploiting the geometrical information contained in the datasets. This method provides an alternative to complex 3D matching algorithms since the implementation of 2D correlation algorithms is much simpler and less time consuming. In the case of landslides not covered by dense vegetation, the proposed approach is accurate for the determination of 3D displacements. The errors related to the approach itself is negligible compared to the instrumental and co-registration errors. The strongest limitation of the approach is due to the development of strong deformation rates between the TLS acquisition.

The kinematics of the front of the Super-Sauze landslide is determined. The obtained displacements are in perfect agreement with the displacements computed with the ICP algorithm and the displacements derived from dGPS surveys. The 2D strain analysis allowed detecting different kinematic patterns which are in good agreement with the surface morphology (fissuring).

Additional efforts are necessary to adapt the method to different acquisition configurations and to integrate in an optimal way the displacement fields obtained from different view points. Nevertheless, the proposed approach could be tested to monitor different kinds of slow geomorphological processes with low (e.g. centimetric) deformation rates and characterized with a sufficiently textured surface (e.g. ice and rock glacier, creeping slopes, inflation of volcanic slopes). The approach can also be adapted for detecting low deformation rates of rock instabilities, because the plastic deformations of the objects (rock compartments) are less important than in soils. The processing chain could be setup in an automatic routine that can be potentially used in permanent monitoring systems.

Acknowledgements

This work was supported by the European Commission through the Marie Curie Research and Training Network '*Mountain Risks: from prediction to management and governance*' (FP6, MCRTN-035798; 2007–2010), and partly through the Large-scale integrating project '*SafeLand: Living with landslide risk in Europe*' (FP7; 2009–2012).

References

Abellán, A., Jaboyedoff, M., Oppikoffer, T., Vilaplana, J.M., 2009. Detection of millimetric deformation using a terrestrial laser scanner: experiment and application to a rockfall event. Nat. Hazards Earth Syst. Sci. 9, 365–372.
Aryal, A., Brooks, A.B., Reid, M.E., Bawden, G.W., Pawlak, G., 2012. Displacement fields form point cloud data: application of particle imaging velocimetry to landslide geodesy. J. Geophys. Res. 117 (F1), 1–15.
Avian, M., Kellerer–Pirklbauer, A., Bauer, A., 2009. LiDAR for monitoring mass movements in permafrost environments at the cirque Hinteres Langtal, Austria, between 2000 and 2008. Nat. Hazards Earth Syst. Sci. 9, 1087–1094.
Bauer, A., Paar, G., Kaufmann, V., 2003. Terrestrial laser scanning for rock glacier monitoring. In: Phillips, M., Springman, S.M., Arenson, L.U. (Eds.), Proceedings of the Eighth International Permafrost Conference, vol. 1. Zurich, Balkema, pp. 55–60.
Besl, P., McKay, N., 1992. A method for registration of 3-D shapes. IEEE Trans. Pattern Anal. Mach. Intell. 14, 239–256.
Bitelli, G., Dubbini, M., Zanutta, A., 2004. Terrestrial laser scanning and digital photogrammetry techniques to monitor landslides bodies. ISPRS – Int. Arch. Photogram. Remote Sens. Spatial Inform. Sci. 35, 246–251.
Casson, B., Delacourt, C., Allemand, P., 2005. Contribution of multi-temporal sensing images to characterize landslide slip surface – application to the La Clapière landslide (France). Nat. Hazards Earth Syst. Sci. 5, 425–437.
Chambon, G., (Ph.D. Thesis) 2003. Caractérisation expérimentale du frottement effectif des zones de faille. Université Paris XI Orsay, Paris.
Chen, Y., Medioni, G., 1992. Object modelling by registration of multiple range images. Image Vis. Comput. 10 (3), 145–155.
Corripio, J.G., 2004. Snow surface albedo estimations using terrestrial photography. Int. J. Remote Sens. 25 (24), 5705–5729.
Debella-Gilo, M., Kaab, A., 2011. Sub-pixel precision image matching for measuring surface displacements on mass movements using normalized cross-correlation. Remote Sens. Environ. 115 (1), 130–142.
Delacourt, C., Allemand, P., Berthier, E., Raucoules, D., Casson, B., Grandjean, P., Pambrun, C., Varel, E., 2007. Remote-sensing techniques for analysing landslide kinematics: a review. Bull. Soc. Geol. 178 (2), 89–100.
Deseilligny, M.-P., Belveaux, J., Choqueux, G., Deveau, M., Girod, L., 2013. MicMac, Apero and Other Beverages in a Nutshell. Edition ENSG, Marne-la-Vallée.
Duffy, G.P., Hughes-Clarke, J.E., 2005. Application of spatial cross correlation to detection of migration of submarine sand dunes. J. Geophys. Res. 110, 1–11.
Duffy, G.P., Hughes-Clarke, J.E., Parrott, R. , 2004. Application of current measurement and time lapsed bathymetric multi beam surveying to investigation of a banner bank, Mispec Bay, New Brunswick, Canada. In: Hulscher, S.J.M.H., Garlan, T., Idier, D. (Eds.), Marine Sandwave Dynamics and River Dune Dynamics II, International Workshop. Univ. of Twente, Enschede, Netherlands, pp. 72–79.
Gruen, A., Akca, D., 2005. Least squares 3D surface and curve matching. ISPRS J. Photogram. Remote Sens. 59 (3), 151–174.
Hild, F., 2003. Mesure de champs de déplacement par corrélation d'images et applications en mécanique des solides. Notes de cours, IPSI. Laboratoire de Mécanique et Technologie, CNRS, Université Paris 6, France.
Hiremagalur, J., Yen, K.S., Akin, K., Bui, T., Lasky, T.A., Ravani, B., 2007. Creating Standards and Specifications for the Use of Laser Scanning in CalTrans Projects. Technical Report F/CA/RI/2006/46. California Department of Transportation, University of California, Davis, USA.
Hodge, R., Brasington, J., Richards, K., 2009. In situ characterization of grain-scale fluvial morphology using terrestrial laser scanning. Earth Surf. Process. Landf. 34, 954–968.
InnovMetric, 2009. PolyWorks User's Manual – 3-D scanner and 3-D digitizer software. InnovMetric Software Inc. http://www.innovmetric.com/
Jaboyedoff, M., Oppikofer, T., Abellan, A., Derron, M.-H., Loye, A., Metzger, R., Pedrazzini, A., 2012. Use of LiDAR in landslide investigations: a review. Nat. Hazards 61 (1), 5–28.

Kasperski, J., Delacourt, C., Allemand, P., Potherat, P., Jaud, M., Varrel, E., 2010. Application of a terrestrial laser scanner (TLS) to the study of the Séchilienne Landslide (Isère, France). Remote Sens. 2 (12), 2785–2802.
Kraus, K., Waldhäusl, P., 1994. Photogrammetry, Fundamentals and Standard Processes. Hermès, Paris.
LePrince, S., Berthier, E., Ayoub, F., Delacourt, C., Avouac, J.-P., 2008. Monitoring earth surface dynamics with optical imagery. EOS 89, 1–5.
Lewis, J.P., 1995. Fast Normalized Cross-Correlation. Vision Interface 95. Canadian Image Processing and Pattern Recognition Society, PPRS, Québec, pp. 120–123.
Lichti, D.D., Jamtsho, S., 2006. Angular resolution of terrestrial laser scanners. Photogramm. Rec. 21, 141–160.
Lindenberg, R., Pfeifer, N., 2005. A statistical deformation analysis of two epochs of terrestrial laser data of a lock. In: Proceedings of the Seventh Conference on Optical 3-D Measurement Techniques, vol. 2, Vienna, Austria, 3–5 October 2005, pp. 61–70.
Liu, L., 2008. A rotation angle calculation method about bearing images based on edge image correlation. Comput. Sci. 5226, 1047–1055.
Malet, J.-P., (Ph.D. Thesis) 2003. Les glissements de type écoulement dans les marnes noires des Alpes du Sud. Morphologie, fonctionnement et modélisation hydromécanique. Université Louis Pasteur, Strasbourg.
Malet, J.-P., Laigle, D., Remaître, A., Maquaire, O., 2005. Triggering conditions and mobility of debris-flows associated to complex earthflows. Geomorphology 66 (1–4), 215–235.
Malet, J.-P., Maquaire, O., Calais, E., 2002. The use of global positioning system techniques for the continuous monitoring of landslides. Geomorphology 43, 33–54.
Monserrat, O., Crosetto, M., 2008. Deformation measurement using terrestrial laser scanning data and least squares 3D surface matching. ISPRS J. Photogram. Remote Sens. 61 (1), 142–154.
Nagashima, S., Ito, K., Aoki, T., Ishii, H., Kobayashi, K., 2007. A high-accuracy rotation estimation algorithm based on 1D phase-only correlation. Comput. Sci. 4633, 210–221.
Niethammer, U., James, M.R., Rothmund, S., Travelletti, J., Joswig, M., 2012. UAV-based remote sensing of the Super-Sauze landslide: evaluation and results. Eng. Geol. 128, 2–11.
Niethammer, U., Rothmund, S., James, M.R., Travelletti, J., Joswig, M., 2010. UAV-based remote sensing of landslides. Int. Arch. Photogram. Remote Sensing Spatial Info. Sci. 38 (5), 496–501.
Oppikofer, T., Jaboyedoff, M., Kreusen, H.-R., 2008. Collapse at the eastern Eiger flank in the Swiss Alps. Nat. Geosci. 8, 531–535.
Oppikofer, T., Jaboyedoff, M., Blikra, L., Derron, H., Metzger, M.H.R., 2009. Characterization and monitoring of the Aknes rockslide using terrestrial laser scanning. Nat. Hazards Earth Syst. Sci. 9, 1003–1019.
Pan, B., Asundi, A., Xie, H., Gao, J., 2009. Digital image correlation using iterative least squares and pointwise least squares for displacement field and strain field measurements. Opt. Lasers Eng. 47, 865–874.
Petrie, G., Toth, C.K., 2008. Terrestrial laser scanners. In: Shan, J., Toth, C.K. (Eds.), Topographic Laser Ranging and Scanning: Principles and Processing. CRC Press, Boca Raton, pp. 87–126.
Picarelli, L., Urciuoli, G., Ramondini, M., Comegna, L., 2005. Main features of mudslides in tectonised highly fissured clay shales. Landslides 2, 15–30.
Pollard, D., Fletcher, C., 2010. Fundamentals of Structural Geology. Cambridge University Press, Cambridge.
Press, W.H., Flannery, B.P., Teukolsky, S.A., Vetterling, W.T., 1997. Numerical Recipes in C, The Art of Scientific Computing, second ed. Cambridge University Press, New York.
Prokop, A., Panholzer, H., 2009. Assessing the capability of terrestrial laser scanning for monitoring slow-moving landslides. Nat. Hazards Earth Syst. Sci. 9, 1921–1928.
Raffel, M., Willert, C.E., Wereley, S.T., Kompenhans, J., 2007. Particle Image Velocimetry: A Practical Guide. Oxford University Press, New York.
Savage, W.Z., Smith, W.K., 1986. A Model for the Plastic Flow of Landslides. US Geological Survey Professional Paper, vol. 1385, 32 pp.
Schürch, P., Densmore, A.L., Rosser, N., Lim, M., McArdell, B., 2011. Detection of surface change in complex topography using terrestrial laser scanning: application to the Illgraben debris-flow channel. Earth Surf. Process. Landf. 36, 1847–1859.
Schwalbe, E., Maas, H.-G., Dietrich, R., Ewert, H., 2008. Glacier velocity determination from multi temporal terrestrial long range scanner point clouds. ISPRS – Int. Arch. Photogram. Remote Sens. Spatial Inform. Sci. XXXVII (Pt B5).
Slob, S., Hack, R., 2004. 3D terrestrial laser scanning as a new field measurement and monitoring technique. In: Hack, R., Azzam, R., Charlier, R. (Eds.), Engineering Geology for Infrastructure Planning in Europe: A European Perspective. Lecture notes in Earth Sciences, 104. Springer, Berlin, pp. 179–189.
Sturzenegger, M., Stead, D., 2009. Quantifying discontinuity orientation and persistence on high mountain rock slopes and large landslides using terrestrial remote sensing techniques. Nat. Hazards Earth Syst. Sci. 9, 267–287.
Teza, G., Galgaro, A., Zaltron, N., Genevois, R., 2007. Terrestrial laser scanner to detect landslide displacement fields: a new approach. Int. J. Remote Sens. 28 (16), 3425–3446.
Teza, G., Pesci, A., Genevois, R., Galgaro, A., 2008. Characterization of landslide ground surface kinematics from terrestrial laser scanning and strain field computation. Geomorphology 97 (3–4), 424–437.
Travelletti, J., Delacourt, C., Toussaint, R., Allemand, P., Malet, J.-P., Schmittbuhl, J., Bastard, M., 2012. Correlation of multi-temporal ground-based images for landslide monitoring: application, potential and limitations. ISPRS – Int. Soc. Photogramm. Remote Sens. 70, 39–55.
Travelletti, J., Malet, J.-P., 2012. Characterization of the 3D geometry of flow-like landslides: a methodology based on the integration of multi-source data. Eng. Geol. 128, 30–48.
Travelletti, J., Oppikofer, T., Delacourt, C., Malet, J.-P., Jaboyedoff, M., 2008. Monitoring landslide displacements during a controlled rain experiment using a long-range terrestrial laser scanning (TLS). ISPRS – Int. Arch. Photogram. Remote Sens. Spatial Inform. Sci. XXXVII (Pt B5), 485–490.
van Asch, Th.W.J., Malet, J.-P., van Beek, L.P.H., 2006. Influence of landslide geometry and kinematics deformation to describe the liquefaction of landslides: some theoretical considerations. Eng. Geol. 88, 59–69.
Vosselman, G., Maas, H.-G., 2010. Airborne and Terrestrial Laser Scanning. Whittles Publishing, Dunbeath.
Weber, D., Herrmann, A., 2000. Contribution of digital photogrammetry in spatio-temporal knowledge of unstable slopes: The example of the Super-Sauze landslide (Alpes-de-Haute-Provence, France). Bull. Soc. Géologique de France 171 (6), 637–648.
White, D.J., Take, W.A., Bolton, M.D., 2003. Soil deformation measurement using particle image velocimetry (PIV) and photogrammetry. Geotechnique 53 (7), 619–631.